NATIONAL ENERGY TECHNOLOGY LABORATORY

OIL & GAS

Hydrate-Bearing Clayey Sediments: Morphology, Physical Properties, Production and Engineering/Geological Implications

Final Scientific/ Technical Report

Project / Reporting Period: 10/1/2012 to 9/30/2017

Date of Report Issuance: February 2018

DOE Award Number: DE-FE0009897

Principal Investigators / Submitting Organization

Sheng Dai
Georgia Institute of Technology
DUNS #: 097394084
Atlanta, GA 30332
+001-(404) 385 – 4757
sheng.dai@ce.gatech.edu

J. Carlos Santamarina
Formerly at Georgia Institute of Technology
Now at King Abdullah University of Science and Technology
+966-(0) 12 - 8087262
carlos.santamarina@kaust.edu.sa

Prepared for:
United States Department of Energy
National Energy Technology Laboratory

Submission date: 12/30/2017

U.S. DEPARTMENT OF ENERGY | NATIONAL ENERGY TECHNOLOGY LABORATORY

Office of Fossil Energy

DISCLAIMER:

Table of Contents

Table of Figures

List of Tables

Abstract

Fine-grained sediments host more than 90 percent of global gas hydrate accumulation. However, hydrate formation in clay-dominated sediments is less understood and characterized than other types of hydrate occurrence. There is an inadequate understanding of hydrate formation mechanisms, segregation structures, hydrate lens topology, system connectivity, and physical macro-scale properties of clay-dominated hydrate-bearing sediments. This situation hinders further analyses of the global carbon budget as well as engineering challenges/solutions related to hydrate instability and production. This project studies hydrate-bearing clay-dominated sediments with emphasis on the enhanced fundamental understanding of hydrate formation and resulting morphology, the development laboratory techniques to emulate natural hydrate formations, the assessment of analytical tools to predict physical properties, the evaluation of engineering and geological implications, and the advanced understanding of gas production potential from fine-grained sediments.

Executive Summary

Methane hydrates in marine and permafrost sediments are potential energy resources. The total amount of carbon trapped in gas hydrate exceeds the sum of all other forms of conventional fossil fuels. The dissociation of methane hydrates can affect the climate and cause ground subsidence and seafloor landslides. Over 90% percent of the global hydrate mass is found in fine-grained sediments which have not yet been extensively studied. This research project focuses on the fundamental understanding of hydrate formation and dissociation in fine-grained sediments, as well as the associated physical processes. The discussion ranges from the particle-scale to the macro-scale, including the shift in the phase boundary associated to curvature effects, the particle-displacive morphology, diffusion induced Leisegang bands and two hydrate formation patterns in gas-filled openings. An array of laboratory techniques that emulate natural gas hydrate formations have been developed in this project. The experimental results illustrate the hydrate formation process via different strategies that aim to accelerate the gas supply to the hydrate formation front. In addition, the evaluation and characterization of the hydrate-saturation dependent physical properties using experimental, numerical, and analytical tools are investigated addressing the impacts of the segregated morphology of hydrates in fine-grained sediments and the change in physical properties induced by cryogenic suction. The project also explored the potential methods to produce gas from hydrate-bearing fine-grained sediments and associated geomechanical responses during gas production from hydrate-bearing fine-grained sediments. This project will add significant data and knowledge to the body of hydrates science. An enhanced understanding of the occurrence and behavior of hydrates in clay-dominated sediments will inform discussions of both the role of hydrates in the global carbon cycle and the potential feasibility of production from a portion of the hydrate resource base not currently considered producible.

1. Introduction

Hydrate-bearing sands are considered most favorable for future gas production (Boswell, 2009; Boswell and Collett, 2011). However, over 90% percent of the global hydrate mass is found in fine-grained sediments (Boswell and Collett, 2006). Thus, hydrate-bearing clays can play a critical role in the potential of methane hydrate as a future energy source and in the natural environment. Yet, there has been minimal research in hydrate-bearing fine-grained sediments to date.

Gas hydrate grows in natural sediments by either filling the pores or segregating the grains. The mesoscale hydrate morphology is determined by the effective stress σ' and the characteristic fine grain size d10, which inherently reflect the relative magnitude of the skeleton and capillary forces at particle-level during hydrate crystal growth (Dai et al., 2012). Gas hydrate tends to be segregated in finer sediments subjected to lower stress, in which capillarity outweighs the skeleton force, and most segregated hydrate found in fine-grained sediments in nature tend to form interconnected networks, such as in the Krishna-Godavari Basin (Collett et al., 2008) and the Ulleung Basin (Yun et al., 2011a).

Fine-grained sediments inherently imply small pore sizes, high specific surface, and low hydraulic conductivity. Consequently, the contribution of advection to methane transport in fine-grained sediments is very low, and diffusion is extremely slow (Xu and Ruppel, 1999). Capillary effects are pronounced in small pores. This hinders both crystal formation and gas flow. In addition, the compressibility of fine-grained sediments implies high volume changes when subject to variations in effective stress, cryogenic suction or gas pressure.

Studies on hydrate-bearing fine-grained sediments are very limited, in part due to the emphasis on hydrate-bearing sands i.e., the apex of the resource pyramid (Boswell, 2009), but also because of laboratory challenges in forming gas hydrates in clays as the way nature does it. Methane concentration in hydrate (1:~7) is much higher than methane solubility in water (1:~700 at SPT), hence hydrate formation is transport-limited in water-saturated sediments. Given the low conductivity of clayey sediments, advection is very slow and in fact, diffusive transport may prevail.

Molecular dynamics simulations show partial preservation of the methane hydrate structure next to the mineral surface and the formation of hydrogen-bonds (Cygan et al., 2004): the methane molecule is enclosed between the hexagonal oxygen ring on the clay surface and a clathrate-like water structure normal to the clay platelet (Park and Sposito, 2003). The size and charge of interlayer cations alter the configuration of adsorbed water molecules (Sposito et al., 1999). Hydrate nucleation is facilitated in clay suspensions (Cha et al., 1988). Yet, the small pore size in clayey sediments inhibits hydrate formation

(Clennell et al., 1999a). Field and laboratory techniques provide a wide range of resolution in the characterization of hydrate-bearing clayey sediments, including micro-CT scanning (Rees et al., 2011), electrical resistivity (Cook et al., 2010; Cook et al., 2012), and seismic imaging (Lee and Collett, 2009; Riedel et al., 2010). The controlled synthesis of methane hydrate in sediments is challenging due to the low solubility of methane in water. This situation is exacerbated in clayey sediments where methane transport may be diffusion limited, and where the scale of devices must allow for hydrate segregation and lens formation. THF and ice analogs (Watanabe et al., 2006) used to explore lensing have fundamental differences (e.g., methane-transport limited vs. heat-diffusion limited), but do share some important underlying phenomena (e.g., capillary control, cryogenic suction and stress-field effects).

This project centers on hydrate-bearing clayey sediments. The research combines in-depth understanding of the physics of nucleation and growth (chemo-mechanical coupling), new analytical/numerical tools to explore physical properties, various experimental strategies to form hydrate in a manner that emulates the interconnected morphologies observed in natural sediments complemented with extensive monitoring and high-resolution imaging, and analytical/numerical investigations to identify optimal strategies for gas production and their inherent limitations. Specifically, efforts have been placed on:

- fundamental understanding of hydrate formation and ensuing morphology in clayey sediments
- development of robust laboratory protocols to form hydrate (network) in clayey sediments
- assessment and prediction of fundamental physical properties of hydrate-bearing clayey sediments considering the innate heterogeneity and anisotropy in these sediments
- a possible paradigm shift in gas production from these sediments
- evaluation of engineering and geological implications to the settlement, geomechanical stability, and the carbon cycle.

Salient findings are presented in the following sections.

2. Formation, distribution, and morphology

2.1 Minimum pore size for nucleation

Methane solubility in water is 0.102mol/kg (5MPa, 273.15K), the equivalent to one methane molecule in 550 water molecules. By contrast, there is one methane molecule per 6 to 7.4 water molecules present in the methane hydrate structure (Sloan and Koh, 2008). Therefore, methane hydrate formation from dissolved gas is inherently gas limited. Dissolved methane transport involves diffusive and advective contributions. The contribution of advective transport decreases in sediments with a high specific surface and low hydraulic conductivity, and hydrate tends to accumulate in coarse clean sands. Small pores affect the phase boundary of gas hydrate (Handa and Stupin, 1992; Seshadri et al., 2001; Uchida et al., 1999a).

The critical nucleation size for methane hydrate ranges from 14.5-170Å (Baez and Clancy, 1994; Westacott and Rodger, 1998). Consider an enclosed pore with a solute concentration of initially c_i, and post-nucleation c_p which is in equilibrium the formed crystal. The critical pore diameter d_p is

$$d_p = d_c \sqrt[3]{\frac{1-c_p}{c_i-c_p}}, \tag{2.1}$$

where d_c is the critical nuclei size (Figure 2.1a). Assuming c_p is 1.34% (equivalent to 0.102 mol/kg) and $c_i = 1.2c_p$. Therefore, $d_p \approx 7.2d_c$ according to Equation 2.1. For a critical nuclei size d_c = 40Å, the minimum pore size to allow methane hydrate nucleation should be d_p = 288Å. Figure 2.1b shows the pore diameter in three types of clays from Georgia under nominal stress. More than 30% by volume of the pores are smaller than 288Å in Illite. This analysis highlights the low probability of stable hydrate nucleation in small pores and preferential nucleation in large pores as the diffusive transport between the pores may not be fast enough to sustain an incipient nucleation growth.

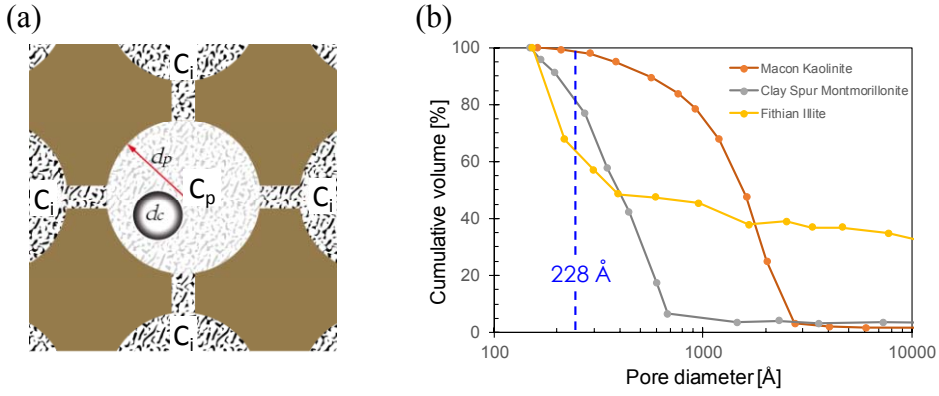

Figure 2.1 Analyses of critical pore size for hydrate nucleation. (a) Schematic illustration of

crystal nucleation in a pore. (b) Pore diameter distribution in three types of clays under nominal stress.

2.2 Gas hydrate phase boundary in fine-grained sediments

The hydrate phase boundary is different in fine-grained sediments to that of bulk hydrate.

The Kelvin and Gibbs-Thomson equations are equivalent to each other under ideal conditions in single substance condensation processes. The integrated form of the Clapeyron equation is the connection between these two equations (McDonald, 1953).

$$\text{Kelvin's equation: } \ln\frac{P_g}{P_{g0}} = \kappa_{wg}\Gamma_{wg}\frac{V_m}{R_g T}, \tag{2.2}$$

$$\text{Clapeyron's Equation: } \ln\frac{P_g}{P_{g0}} = \frac{L}{ZR_g}\left(\frac{1}{T_1}-\frac{1}{T_2}\right), \tag{2.3}$$

where P_g is the actual vapor pressure; P_{g0} is the saturated vapor pressure; $\kappa_{wg} = 1/r_1+1/r_2$ is the curvature of the interface and r_1 and r_2 are the principal radii of curvature; Γ_{wg} is the surface tension between the liquid/crystal and its vapor; V_m is the molar volume of the liquid/crystal; R_g=8.314 J/(mol·K) is the gas constant; T is the temperature; L is the molar latent heat of the phase transition; and Z is the gas compressibility. The curvature of the interface $\kappa_{wg} = 2\cos(\theta)/r_t$ when in a cylindrical tube, where θ is the contact angle and r_t is the radius of the capillary tube. These two equations in combined can lead to the equation in an ideal gas case (Z = 1):

$$\text{Gibbs-Thomson's Equation: } \frac{\Delta T}{T_B} = \kappa_{wg}\Gamma_{wg}\frac{1}{H_f \rho_h}, \tag{2.4}$$

where ΔT is the temperature depression from the bulk phase boundary; T_B is the temperature at the bulk phase boundary; H_f is the bulk enthalpy of fusion; ρ_h is the hydrate density.

The phase boundary of methane hydrate involves more than two phases. However, the Clapeyron's equation still applies to the whole system. The volume of gas locked in hydrate dominates the volume change in the hydrate-water-gas system. Therefore, the volume change approximates the gas volume $\Delta V \approx V_g$, so $P\Delta V = PV_g = ZR_g T$. Then the modified Kelvin equation for hydrate by the substitution of Equation 2.4 to 2.3,

$$\ln\frac{P_g}{P_{g0}} = \frac{2\Gamma_{wg}}{r}\frac{V_m}{ZR_g T}. \tag{2.5}$$

Figure 2.2 illustrates the comparison between the estimations of the Gibbs-Thomson and modified Kelvin equations. The two match well under low-pressure conditions but deviate at high-pressures. This is primarily due to the increase in the volume difference between the hydrate and water as the gas density increases.

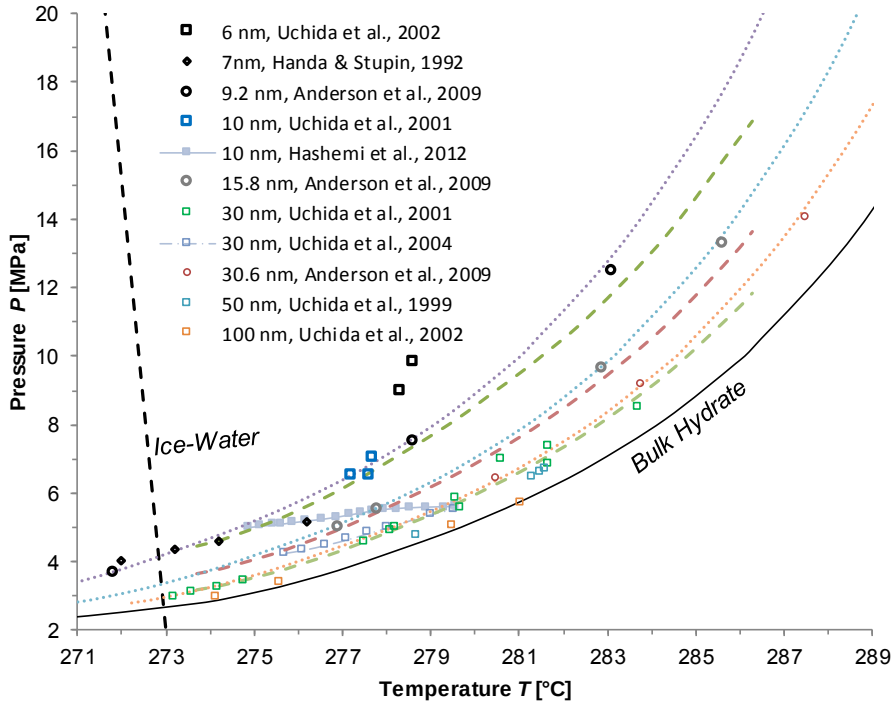

Figure 2.2 Temperature depression due to curvature. The dotted lines are the prediction from the Gibbs-Thomson's equation, and the broken lines demonstrate the estimation from the modified Kelvin's equation.

2.3 Gas hydrate morphology

In capillary tubes. The Laplace equation characterizes capillary pressure between the two phases separated by the interface as

$$P_c = \frac{2\Gamma \cos\theta}{r}. \tag{2.6}$$

As illustrated in Figure 2.3a, the hydrate phase pressure in a saturated tube with diameter d_1 is

$$P_h = u_w + \frac{4\Gamma_{wh} \cos\theta}{d_1}, \tag{2.7}$$

where u_w is the water pressure. At the pore throat with a throat size of d_2, the hydrate phase pressure becomes

$$P_h = u_w + \frac{4\Gamma_{wh}\cos\theta}{d_2}. \tag{2.7}$$

With the presence of gas phase (i.e., unsaturated), the hydrate phase pressure becomes

$$P_h = \left(P_g - \frac{4\Gamma_{wg}\cos\theta_{wg}}{d_1}\right) + \frac{4\Gamma_{wh}\cos\theta_{wh}}{d_1}. \tag{2.8}$$

Note also that as illustrated in Figure 2.3b, the curvature of the interfaces is constrained by pore geometry for a given contact angle (Jang et al., 2016), and that significantly alters the interfacial forces.

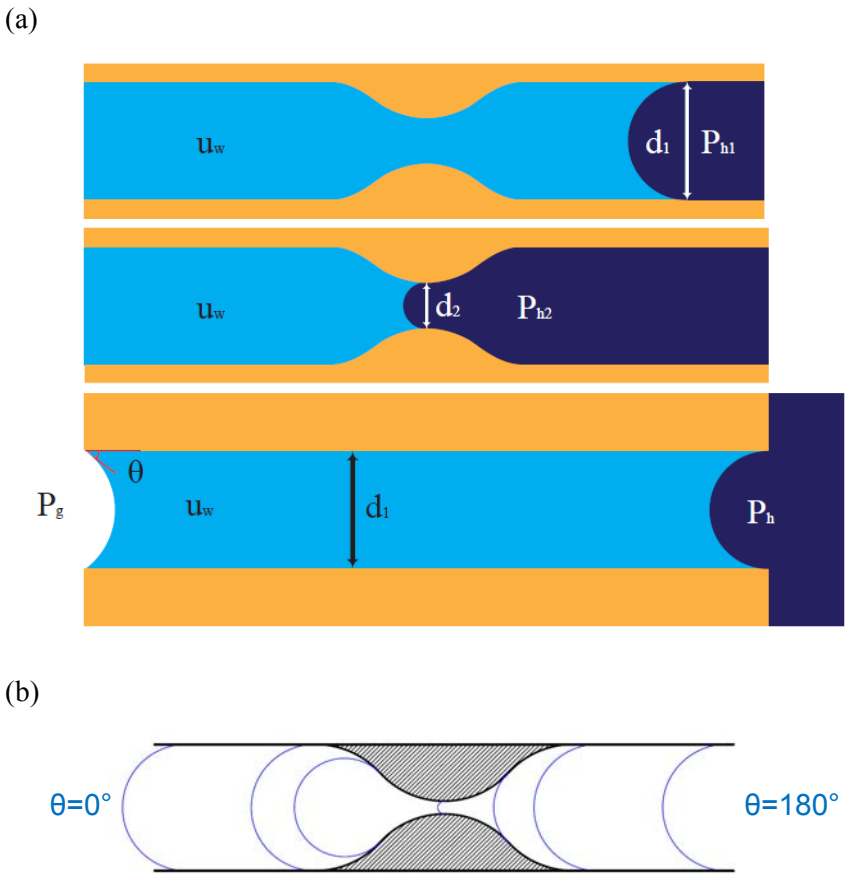

Figure 2.3 Pore-scale equilibrium. (a) Phase pressure in the hydrate-water-mineral systems. (b) Illustration of the pore shape effects on interfacial curvature (Jang et al., 2016).

In sediments. Studies of the pore size effect usually assume that the pore shape does not change during the crystal formation and dissociation processes. However, the pores cannot exist without a container, which creates the separated pore space. A small crystal is in a state of self-reacted equilibrium in bulk water. The strength of the pore wall depends on the tensile strength of the material. However, particulate materials such as non-cemented sediments have no tensile strength. The effective stress then characterizes this pore wall strength. The stress generated by the hydrate crystal growth balances the effective stress in fine-grained marine sediments. Effective stress in the sediments could be much less than the capillary pressure between the crystal and fluid, particularly in shallow marine sediments. Alternatively, the sediments skeleton is not strong enough to constrain the stress induced by the crystal growth. Consequently, crystal growth enlarges the pores. This enlargement process is the mechanism involved in the particle-displacive formation (Figure 2.4). We define the characteristic pore throat size in a particular sediment as d, which corresponds to a characteristic capillary pressure P_{cap} (Laplace equation) and a characteristic temperature depression $\Delta T'$ (Gibbs-Thomson equation).

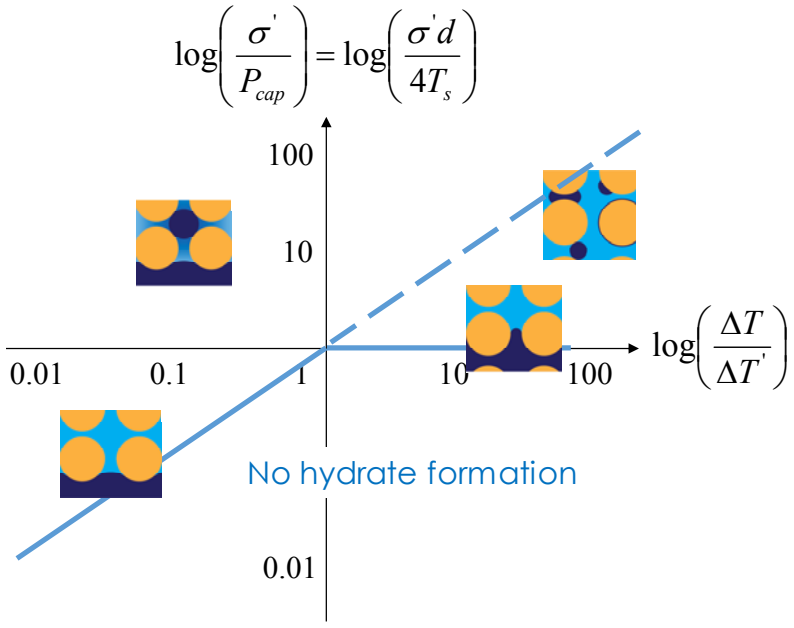

Figure 2.4 Temperature depression, capillary pressure and effective stress dominated hydrate morphology.

Without boundaries. Due to the molecular structure, the crystal lattice subject to certain temperature and pressure conditions favors particular structures that minimize the energy of the system. The energy required to create a surface depends on the surface orientation.

The distance of any stable crystal surface from the center of the crystal is proportional to its surface tension (Adamson and Gast, 1967). For a polyhedron crystal, the equilibrium shape usually coincides with the lattice structure of the crystal. However, natural crystals larger than a particular size do not usually display the most stable shapes, dependent on the formation conditions. In addition, crystal defects such as dislocations and imperfections introduced during the dynamic formation process could alter the morphology. Consequently, crystals do not share identical morphologies due to the variations in formation conditions.

Particle-displacive Crystal Morphology with Boundaries. The sediments contain interconnected water that surrounds the hydrate crystals. Therefore, we assume that the salinity, methane concentrations and other solvents that could alter the phase equilibrium are in the same state in the environment around the hydrate crystal. The assumption only applies when the system is in a state of equilibrium. Consequently, the crystal surface has the same curvature wherever it contacts the water, and there is no deviatoric stress in the crystal. Note that the above assumption does not apply to a dynamic system as the required timescale to diffuse the excluded ion or methane could be longer than the timescale of the dynamic formation and dissociation processes. A hydrate crystal in the sediment is a balloon-like structure that bears the same effective stress and the fluid pressure from all directions. The morphology of the crystal, in this case, reflects the adjacent effective stress distribution in the sediments.

2.4 Formation mechanisms and topology

Gas supply. Methane solubility in water varies, dependent on the presence or absence of gas hydrate in the solution. This variation in solubility induces the formation of a 4mm thick hydrate lens within a 1m thick cubic solution (Jang and Santamarina, 2016). The formation of this amount of hydrate develops with the methane dissolved in the solution and does not involve a long distance supply. The Péclet number decreases with particle and pore size. Therefore, diffusion dominates the mass transfer in fine-grained sediments. The estimated timescale for diffusion-controlled gas hydrate to form a 200-m-thick methane hydrate zone can be up to tens to hundreds of millions of years (Xu and Ruppel, 1999). For laboratory experimental purposes, gas diffuses through a 2-cm-thick specimen over the course of 7 days. The time required is proportional to the squared specimen thickness. However, diffusion is not the only gas supply path into fine-grained sediments. Ocean explorations in a variety of sites report abundant pockmarks on the ocean floor. Pockmarks indicate a historical gas release from the bottom of the ocean (Paull et al., 1995). Furthermore, active gas plumes can coexist with gas hydrate-bearing sediments (Wood et al., 2002). The height of one plume reached 1400m in an extreme case (Gardner

et al., 2009). These observations indicate the extensive and disruptive gas flow through the hydrate stability zone. Additionally, in-situ testing results demonstrate the presence of gas-filled cavities in shallow marine sediments (Sultan et al., 2004). Experimental results in Session 4 illustrate that gas-driven fractures can remain open in consolidated fine-grained sediments when the gas flow ceases.

Diffusion dominated hydrate formation. Hydrate formation by diffusion is a diffusion-reaction process. Similar natural processes create Liesegang bands or rings (Figure 2.5). Methane diffusion through the sediments follows the methane concentration gradient. When the first band of hydrate forms, the ion exclusion increases its concentration near the hydrate formation front. The capillary effect consolidates the nearby sediments and decreases the pore size. The combination of these two effects results in a suppression of hydrate nucleation in the near field. Meanwhile, the hydrate in this condition yields a high methane concentration due to salinity and curvature effects. Therefore, hydrate could independently nucleate and form away from the pre-formed hydrate in areas where the methane concentration is relatively lower. However, these areas contain larger pore sizes and lower ion concentrations. The process continues with successive bands of hydrate and consequently hydrate could form the Liesegang bands.

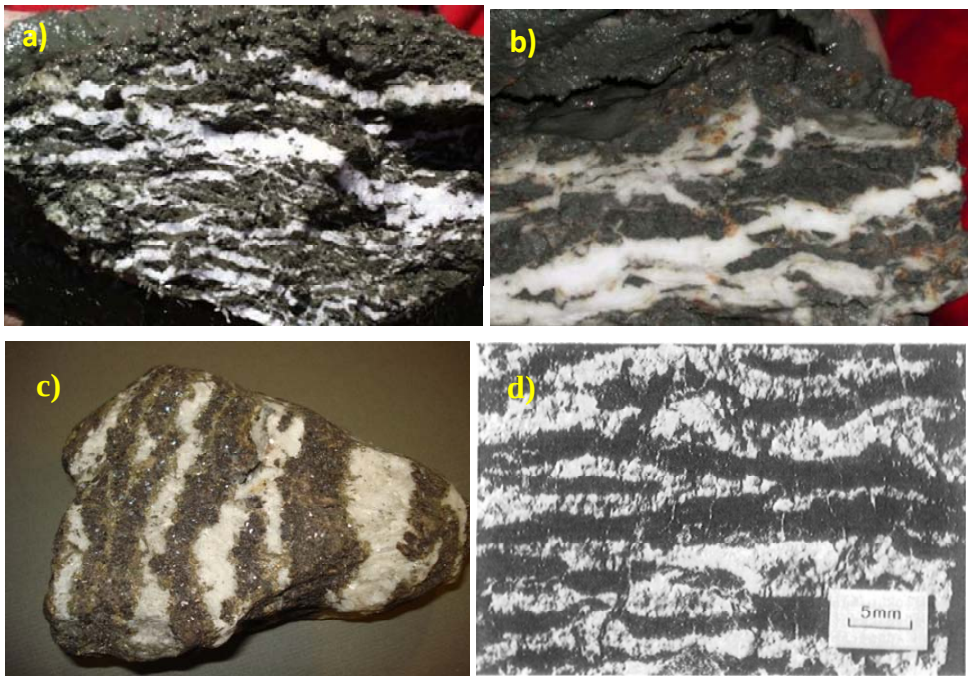

Figure 2.5 Analogue to natural Lisegang bands in ores. a) Hydrate at Hydrate Ridge, GEOMAR, 2012; b) Hydrate at the Gulf of Mexico, GEOMAR, 2012; c) Zinc ores, uwaterloo.ca/earth-sciences-museum; d) Dolomite bands in ores, (Merino, 1984).

Gas-driven fractures formation. The conditions for gas-driven (immiscible fluid) fractures to form in water-saturated sediments are (Figure 2.6):

$$u_w + k_0\sigma_v^{'} \le P_{gas} \le u_w + \sigma_v^{'}, \tag{2.9}$$

$$P_{gas} - u_w \le P_{cap,wg} \tag{2.10}$$

where u_w is the pore water pressure, k_0 is the horizontal stress coefficient, σ'_v is the vertical effective stress, P_{gas} is the gas pressure and $P_{cap,wg} = \kappa_{wg}\Gamma_{wg}$. Equation 2.9 provides the relationship between gas pressure and the overall pressure. If the pore throats in the sediments are sufficiently small, gas will not invade into the sediment pores but will create fractures (Equation 2010).

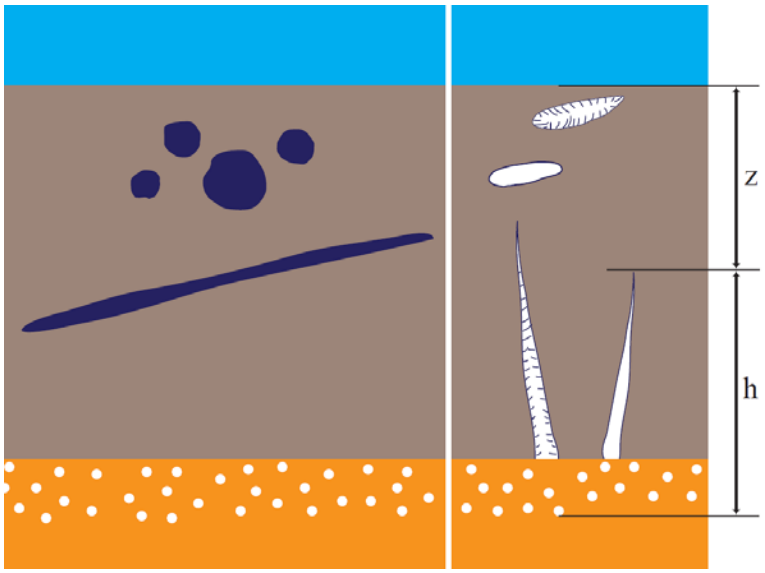

Figure 2.6 Gas supply to the hydrate formation front via diffusion and gas-driven fractures.

Gas driven fracture accelerated hydrate formation. Hydrate forms on the interface between water and gas inside the fracture. The subsequent hydrate growth extracts water from the sediments, which shares the same mechanism as cryogenic suction. The two mechanisms of film and exo-pore patterns could both exist at this stage.

A thin porous hydrate film forms thickens and solidifies on the hydrocarbon-water interface (Taylor et al., 2007; Uchida et al., 1999b). The final long-term methane hydrate film thickness ranges from 20 to 100μm, as the sub-cooling increases from 4 to 13.5°C (Taylor et al., 2007). Further hydrate growth relies on either gas diffusion through this film to the water-hydrate interface or water diffusion through the film to the hydrate-gas interface.

The diffusion coefficient of tritium in natural ice at -10°C is approximately $2\times10^{-11}cm^2/s$ (Ramseier, 1967). This is six orders of magnitude slower than the H_2 diffusion coefficient in liquid water $4.5\times10^{-5}cm^2/s$ (Cussler, 2009), which is already significantly slow. CH_4 diffusion in solid is even slower than tritium due to its larger molecule size. In a worse scenario, if the water in the sediment is not initially saturated with gas, the methane dissolved in the water near the hydrate film diffuses into the far field. The hydrate film then dissolves into the water. This scenario can both occur in the laboratory and natural conditions. The film pattern mechanism in hydrate formation could occur on the hydrocarbon-sediment interface in gas-filled openings (Figure 2.7).

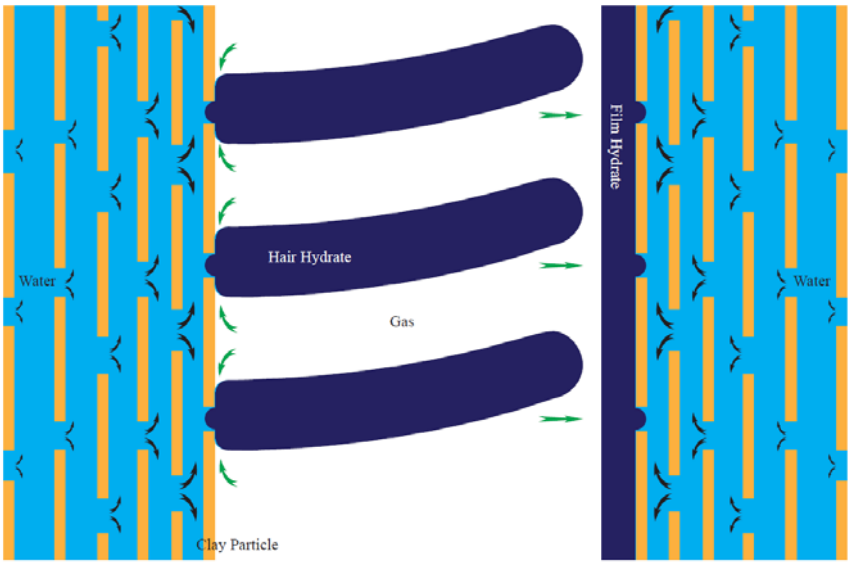

Figure 2.7 Hydrate crystal growth in gas-filled openings. Film and exo-pore patterns of crystal growth.

Laboratory CO_2 hydrate formation experiments in fine-grained sediments demonstrate this film pattern when the film thickness exceeds the resolution of the micro-CT system (details in Session 4). Experimental results do not detect a film pattern hydrate growth thicker than 100μm. The curvature effect shifts the hydrate phase boundary to a lower temperature. Therefore, it is easier to form hydrate outside than within the pores due to the temperature depression. Crystal initially nucleates on the end of the pore, and the subsequent hydrate growth depends on the water supply from the sediment and the gas supply from the gas-filled openings (Figure 2.7). The hydrate formation front is on the interface between the hydrate and water. The capillary pressure between the hydrate and water drives the water supply from the sediment, termed cryogenic suction. Simultaneously, gas-filled openings provide a direct gas supply to the hydrate formation front. The hydrate-phobic

mineral surface tends to repel the hydrate. Consequently, the hydrate automatically rises from the root.

Figure 2.8 illustrates a number of natural examples that result from this pattern. We also observe this pattern in laboratory gas hydrate formation experiments, either on the surface of the fine-grained sediments or within the gas-filled openings (Session 4). This same mechanism produces up to 5cm long crystals in 3 to 4 hours.

Figure 2.8 Natural examples and laboratory illustrations of exo-pore mechanisms. a) Hair ice (Hofmann et al., 2015); b) Frost flower on dittany (MacRae, 2010); c) Needle ice (Credit: Kelvin Freitas); d) Gypsum flower (Credit: Dave Bunnell); e) Gypsum needle (Alonso and Ramon, 2013); f) Hydrate shell (Session 4).

The subsequent gas hydrate formation consumes the gas in the openings and decreases the gas pressure. This process eventually collapses the openings and consolidates the hydrate. Porous hydrates that do not fully solidify frequently exist in shallow marine fine-grained sediments (Sultan et al., 2014). The horizontal stress near the hydrate crystal could be much higher than in the far field, as the cryogenic suction consolidates the sediments. Consequently, the hydrate formation densifies the adjacent sediment. The subsequent gas plume can occur in other sediment locations in zones of sediments with relatively lower strength. This trend continues until the whole field reaches a high hydrate saturation rate.

2.5 Laboratory formation methods

The following strategies have been used to form hydrate in clayey sediments:

- THF hydrate in various clays
- Particle inner pore space utilization (i.e., diatoms)
- Ice-to-hydrate transformation
- Gas injection into the bottom the specimens
- Long-term gas diffusion

All tests conducted are summarized in Table 2.1 with typical pressure-temperature history for various tests shown in Figure 2.9.

Table 2.1 List of experiments conducted

Test No.	Sediment Type	Related Figures	Liquid Content [a]	Hydrate Morphology	Notes
THF Hydrate Experiments					
1	Silica Flour	6	40%	Pore-filling	THF/Water molar ratio= 1/17 Supercooling to 2 °C before hydrate formation
2	Diatom	6	150%	Thin Lenses	
3	Diatom (slow)	6	120%	Lenses	
4	Kaolinite	6	60%	Lenses	
5	Bentonite	6	300%	Lenses & blocks	
Particle Inner Pore Space Utilization (CO2 hydrate)					
6	Diatom	--	0%⇨40%	Small Crystals	Water injection into dry diatom specimen: #6&8 inside and #7 outside hydrate stability field
7	Diatom	--	0%⇨30%	Hydrate Flower	
8	Diatom	--	0%⇨40%	Small Crystals	
Ice-to-Hydrate Transformation (CO2 hydrate)					
9	Kaolinite	--	--	Porous Lens	Ice lens in groove - unsaturated kaolinite
10	Kaolinite	--	60%	Shell	Small sample with D=6 mm, L=20 mm
11	Kaolinite	3	55%	Porous Block	Unsaturated
12	Kaolinite	7	--	Porous Lens	Dry kaolinite with embedded ice lens
13	Hydrophobic Silica	--	--	Porous Lens	Hydrophobic silica with large (#13) and small (#14) embedded ice lens
14	Hydrophobic Silica	7	--	Lenses	
Forced Gas Injection (CO2 hydrate)					
15	Diatom	4	40%	Porous Lens	1. Consolidation pressure: 50 kPa 2. Gas injection from bottom
16	Diatom	--	40%	Porous Lens	
17	Layered Specimen[b]	--	48%	Porous Lens	
18	Layered Specimen[c]	--	48%	Porous Lens	
19	Kaolinite	5	150%	Lens, Shell	Slurry - Gas injection from bottom
20	Kaolinite	--	150%	Lens	
Long Term Diffusion (CO2 hydrate)					
21	Bentonite	--	2000%	Stripped (Hair)	Temperature depression after long-time CO_2 diffusion
22	Bentonite	--	300%	Stripped & Lens	

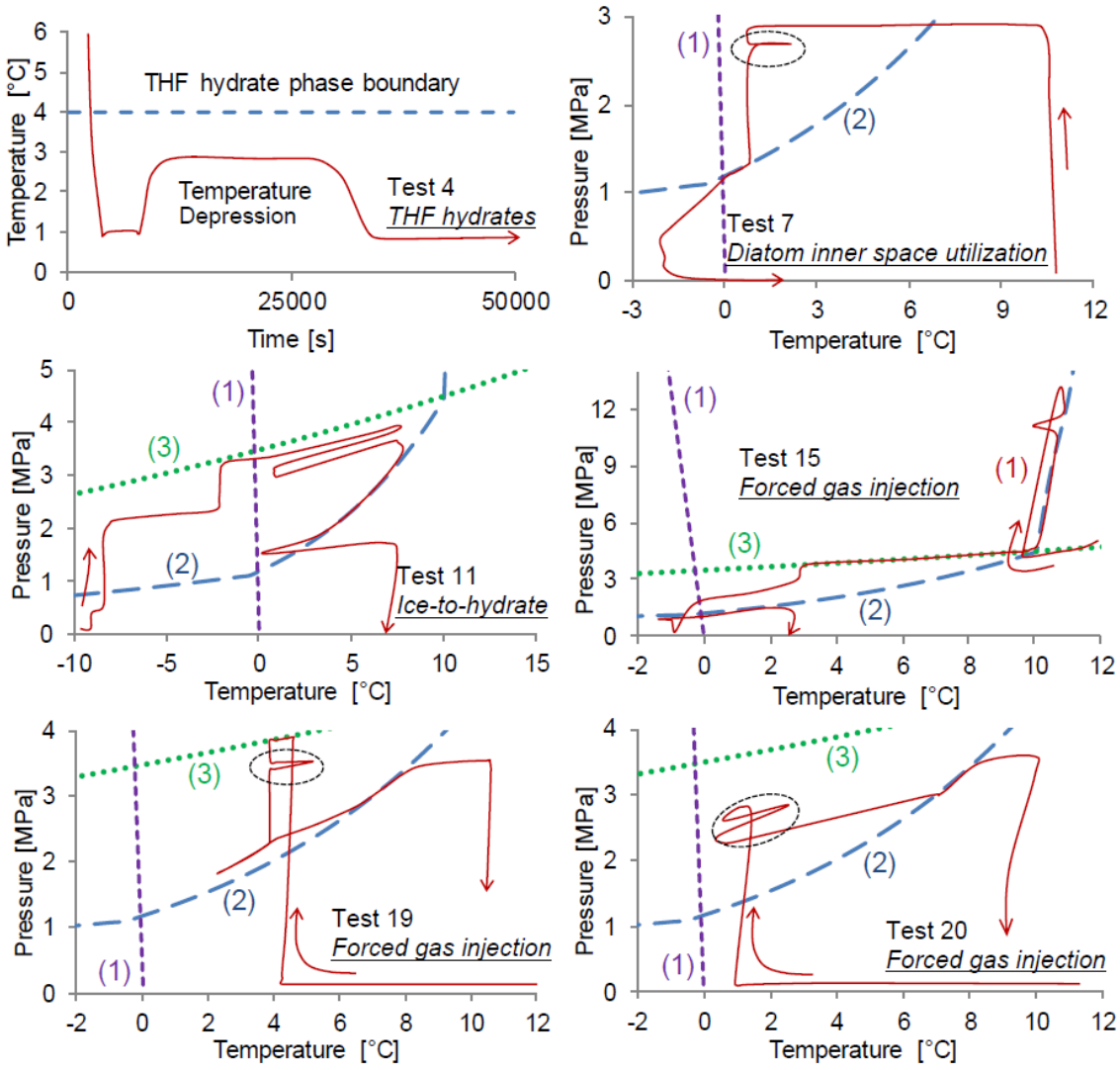

Figure 2.9 Typical P-T trajectories (red lines) for various tests (Test numbers: refer to Table 2.1 for details). Phase boundary is shown for: (1) ice-water, (2) CO2 hydrate and (3) gas-liquid CO2. Exothermic thermal spikes are readily seen in P-T trajectories for Tests 4, 7, 19 and 20.

THF hydrate formation in fines. The miscible characteristic of THF with water enables the hydrate formation without limitation of water or guest molecule supply. Furthermore, THF hydrate formation could occur in atmosphere pressure under 4°C. THF hydrate formation develops in a variety of soil types, under similar thermal conditions (Table 2.1, Tests 1-5). The liquid contents here in the experiments are all slightly above the liquid limit.

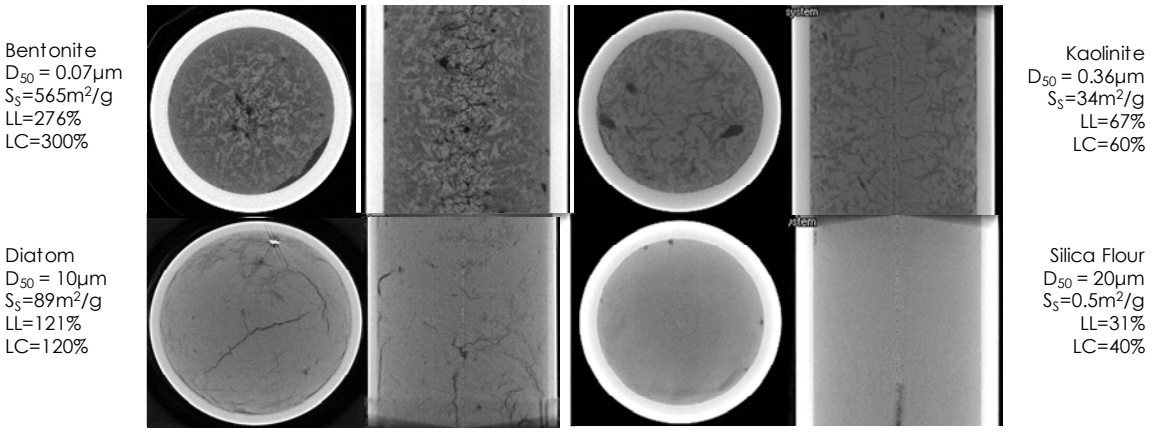

Figure 2.10 CT images of THF hydrate in various of fine-grained sediments.

Hydrate in diatoms. This study recognizes the common coexistence of both hydrate and diatoms in fine-grained sediments (Clennell et al., 1999b; Yun et al., 2011b). Particles in the diatomaceous earth have an inner pore arrangement that is dependent on the diatom species. This series of experiments use the inner space of the diatom particles as the storage space for high-pressure CO_2 gas (Tests 6-8). The injection of water into the specimen then enables hydrate to form with a readily available source of gas already present in the sediment. Consequently, hydrate formation is not limited by the longtime diffusion of guest molecules.

Temperature and pressure trajectories and related analyses indicate that hydrate formed in all diatomaceous earth specimens tested as part of this study. Yet, there are not clear signs of segregated hydrate with the exception of the two hydrates lenses on the top of the specimens (Test 7, Figure 2.11). Small hydrate crystals distributed in pores do not merge into a large segregated hydrate mass that could be distinguished in CT images. In part, this is due to short laboratory timescales that do not allow for Ostwald-ripening, in addition to the generation of high effective stresses in small rigid chambers.

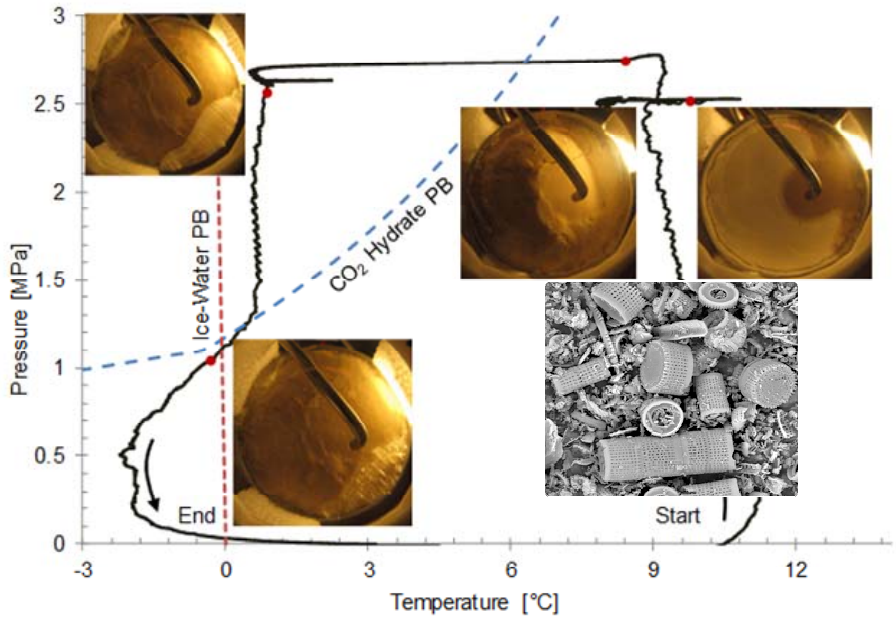

Figure 2.11 Hydrate formation induced during water injection onto an oven dried diatomaceous earth specimen. Water injection starts outside the stability field at a gas pressure P_{gas} =2.5MPa, and T =10.5°C. Selected photographs are shown at PT conditions represented by the filled circle (Test 7, Table 2.1).

Ice-to-hydrate transformation. Ice can serve as gas hydrate nucleation seeds, therefore, the nucleation barrier is reduced. The enthalpy for CO_2 hydrate dissociation is between 57.7 to 63.6kJ/mol, i.e., a mole of CO_2 hydrate is 44g + n18g, where n =5.75-6 (Anderson, 2003). The latent heat in water/ice transformation is 6.05 kJ/mol, equivalent to 34.8-36.3 (6.05 n)kJ per mole of CO_2. Therefore, the ice-hydrate transformation is an exothermic process. In addition, pre-melting commences at the ice crystal surface when T =-33°C. The crystal structure does not fully solidify until temperatures reach 0K (Li and Somorjai, 2007). Once the transformation from ice to hydrate occurs on the pre-melted ice surface, the generated heat melts more ice to release free water for hydrate formation and therefore creates a positive feedback loop to accelerate the process. Ice is introduced into the sediments by the placement of premade ice lenses in dry specimens or freezing unsaturated specimen (Tests 9-14, Figure 2.12). The system then moves into the hydrate stability field initiated by a pressure increase from 33kPa. An ice-to-hydrate transformation occurs as temperatures gradually increase towards ice melting point.

The success of hydrate formation experiments with ice-to-hydrate transformation strategy highly depends on the clear path of gas-supply. The pre-melting of the ice surface and exothermic feature releases free water from the ice crystal lattice and enables water migration to the hydrate formation front or pores in dry sediment. Hydrate formation, which

heavily relies on the relatively slow heat dissipation is slower than the instant water migration process due to capillary suction. Therefore, the final hydrate mass shape reflects the water migration history rather than simply resembling the initial ice lenses.

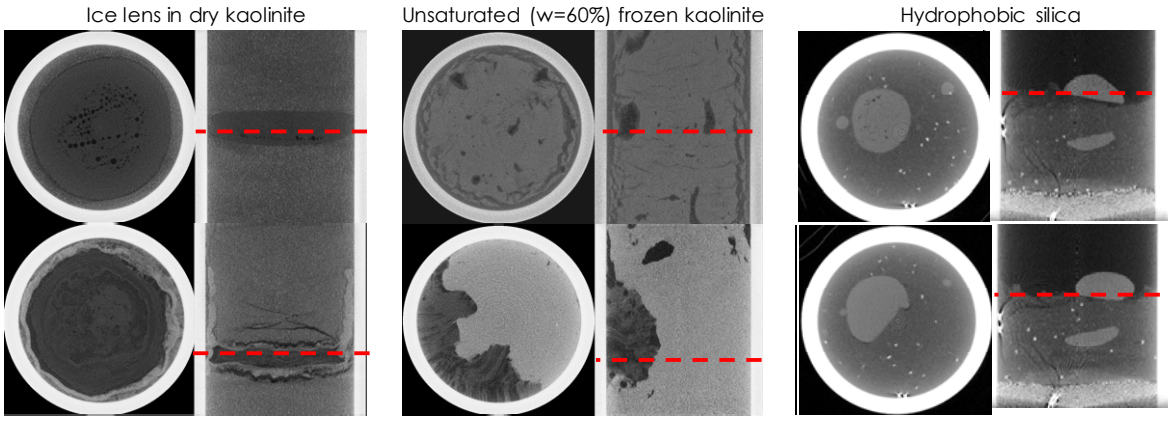

Figure 2.12 CT images of converting ice lens into CO_2 hydrate.

Gas injection. Natural gas plumes on the ocean floor indicate the presence of a free gas paths within the sediment (Gardner et al., 2009). Hydrate formation along the paths depends on the processes of the gas transfer from the fracture and the water supply from the sediments to the hydrate formation front.

These experiments inject CO2 into the water-saturated sediment to cause a gas-driven fracture where hydrate typically nucleates. Specimen preparation in Tests 15 to 18 uses a consolidation pressure of 50kPa, and the effective stress remains during the hydrate formation process through the compressed spring. Gas injection in Test 19 creates bubbles with the volume two to three times of the specimen. Test 20 uses a porous cap on the top of the specimen to reduce the volume expansion of the specimen.

Laboratory produced hydrate that uses gas injection methods aims to emulate natural conditions (Figure 2.13, 2.14, 2.15). The liquid CO_2 represents the gas zone/resource layer under the hydrate-bearing layer, which supplies gas to the hydrate growth within the fine-grained sediments. The gas flow through the openings in fine-grained sediments is a transient process. However, the diffusion of released gas back into the sediment is negligible by laboratory timescales. By contrast, hydrate in fine-grained sediments loses gas to the hydrate formed outside the sediment due to the shifted phase boundary in the pores when effective stress is present. Therefore, a stable gas source under the bottom of the sediments is critical to a successful experiment. The gas resource can also be continuous gas injection from the bottom of the sediments. Yet, backflow and injection needle clogging are

common problems with this technique.

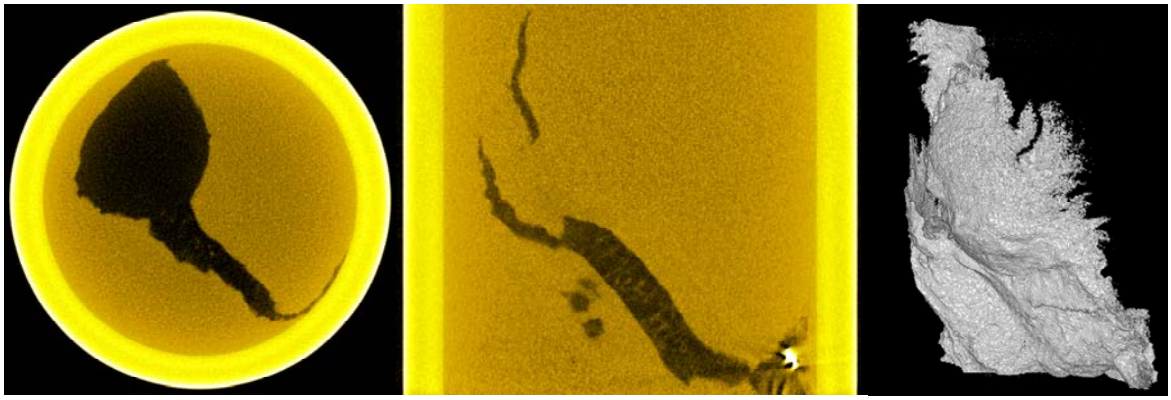

Figure 2.13 Gas injection – open fracture in Kaolinite (D_{50} =0.36µm, S_s = 34m^2/g, LL =67%).

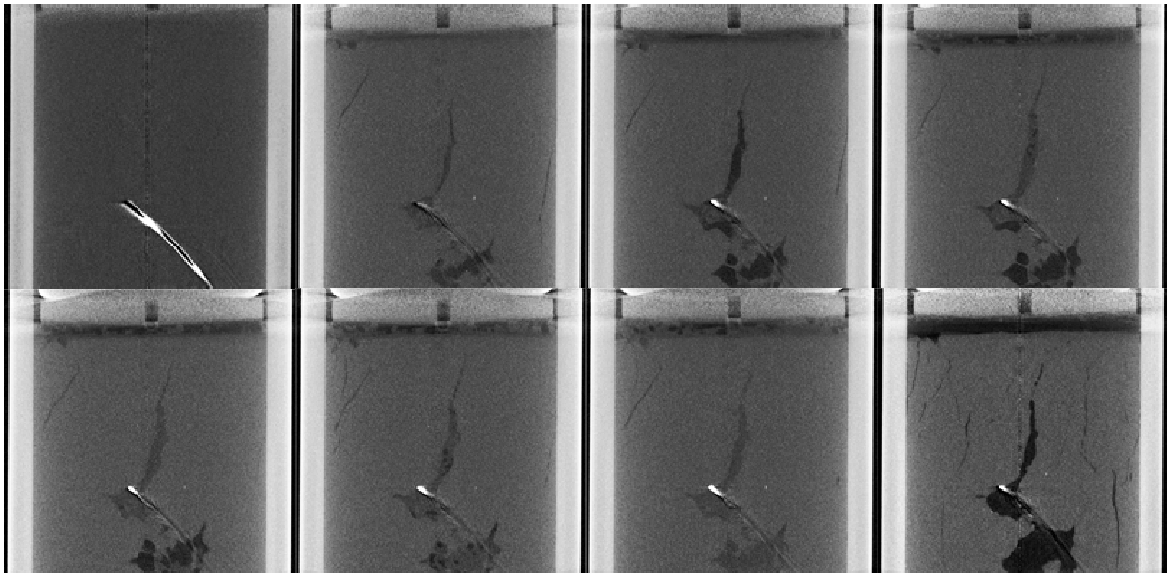

Figure 2.14 Gas injection into diatoms (D_{50} =10µm, S_s = 89m^2/g, LL = 121%).

Figure 2.15 Gas injection – bubbling in the slurry (Test 19 and 20, Table 2.1).

Long-term diffusion. Hydrate formation from CO_2 saturated water in fine-grained sediment is of interest in the study. Diffusion is a crucial component in the gas supply process to saturated fine-grained sediments. Saturation of a 10mm specimen with CO_2 takes place over 7 days. The specimen in Tests 21 and 22 are under pressure no less than 3MPa for 20 days and 10 days respectively before temperature depression.

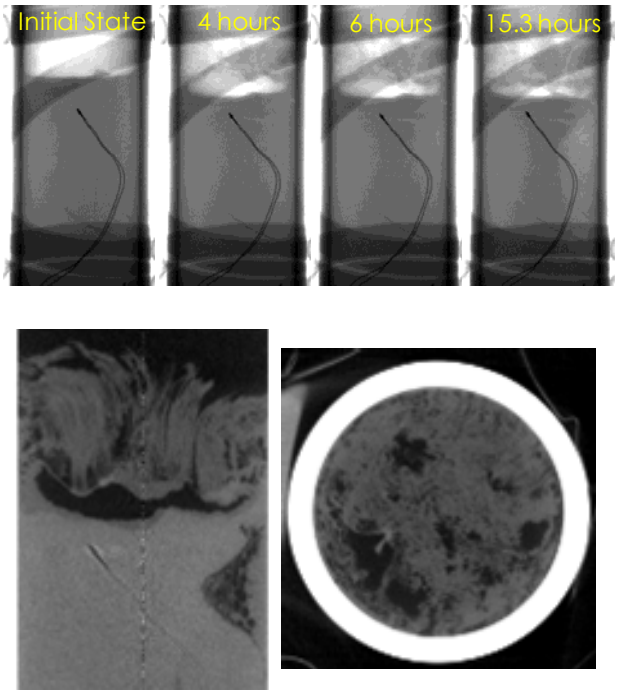

Figure 2.16 CO_2 hydrate formation at the top of and inside a kaolinite paste (Test 22, Table 2.1). The paste is exposed to CO_2 gas at 3.4MPa for 20 days with subsequent temperature decrease to stability field. (a) Evolution in time; (b) Horizontal and vertical slices of the CT after 8 hours.

Reproduction of natural conditions. Laboratory hydrate formation in fine-grained sediments that emulates naturally formed hydrate should create a gas resource inside or underneath the fine-grained sediments. Either a chemical or pressure gradient then drives the gas into the sediment. It is also important to guarantee that there is no quick path for gas to escape from the fine-grained sediments, although this is difficult to achieve in laboratory conditions. A hole with a 1mm diameter can very effectively transport gas through the sediments. Note the hydrate in clayey sediments acts as a buffer during the upward gas migration. The existence of hydrate in sediments is because of gas supply or, a historically supply below the hydrate stability zone. Otherwise, the nonstop loss of gas into the ocean floor from the top of hydrate-bearing sediments would eventually deplete the reservoir. This explains the rareness of natural CO_2 hydrate-bearing sediments.

3. Physical properties of hydrate-bearing clayey sediments

3.1 Hydrate distribution and cryogenic suction

Figure 3.1 presents a collection of X-ray projections and CT slices of sediments recovered using pressure core technology. The bright areas correspond to the low-density hydrate mass. Clearly, the hydrate-sediment interface is not smooth; in fact, the shape of the hydrate mass is quite irregular and jagged.

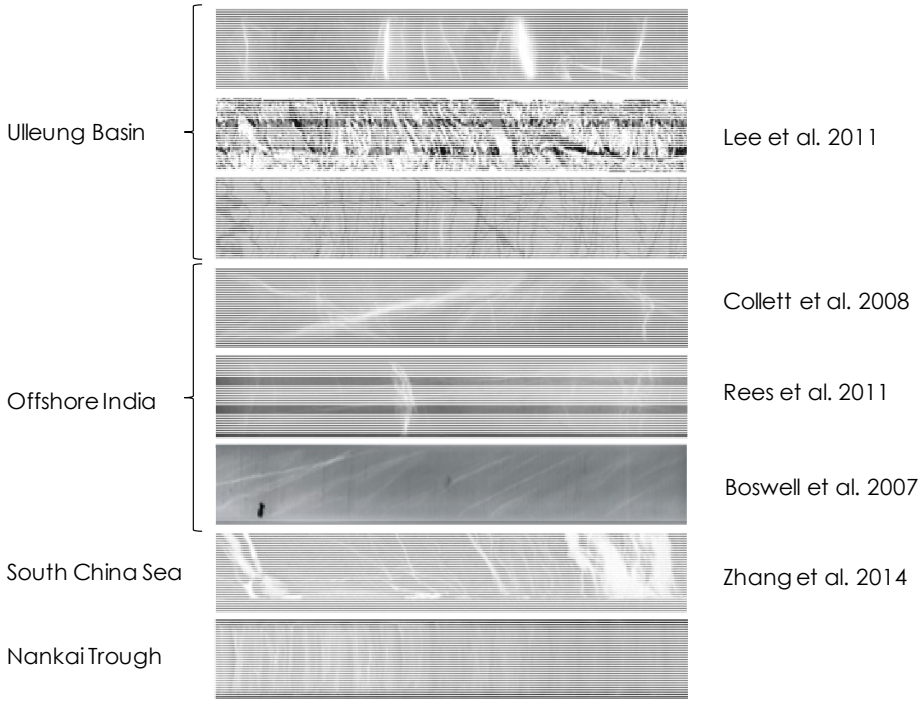

Figure 3.1 X-ray CT images of pressure cores.

Hydrate formation from dissolved methane in fine-grained sediments is a diffusion-limited reaction process. Images in Figure 3.1 exhibit Liesegang band topology (Session 2). Alternatively, hydrate forms in gas-driven fractures and inherits the fracture topology, including its rough edges and uneven propagation fronts (Figure 2.13); these features can explain morphological characteristics observed in Figure 5.1.

Hydrate saturation is defined as the ratio between the hydrate volume and the overall pore space. However, this definition is inadequate for particle-displacive hydrate distributions. Instead, this report defines the hydrate volume fraction V_{Fh}, as the ratio between the volume of hydrate and the total sediment volume.

Cryogenic suction: Over-consolidation. Hydrate formation extracts water from the sediments and causes it to compact or consolidate. Figure 3.2 demonstrates the consolidation effect of cryogenic suction on a kaolinite specimen subject to a freezing front imposed on the upper boundary; the X-ray attenuation coefficient in the sediments is higher near the ice front (top) than in the far field of the cold front (bottom). The pressure of the hydrate mass equilibrates the sum of the pore water pressure and the effective stress. Therefore, the effective stress equals the capillary pressure between the hydrate mass and the pore water.

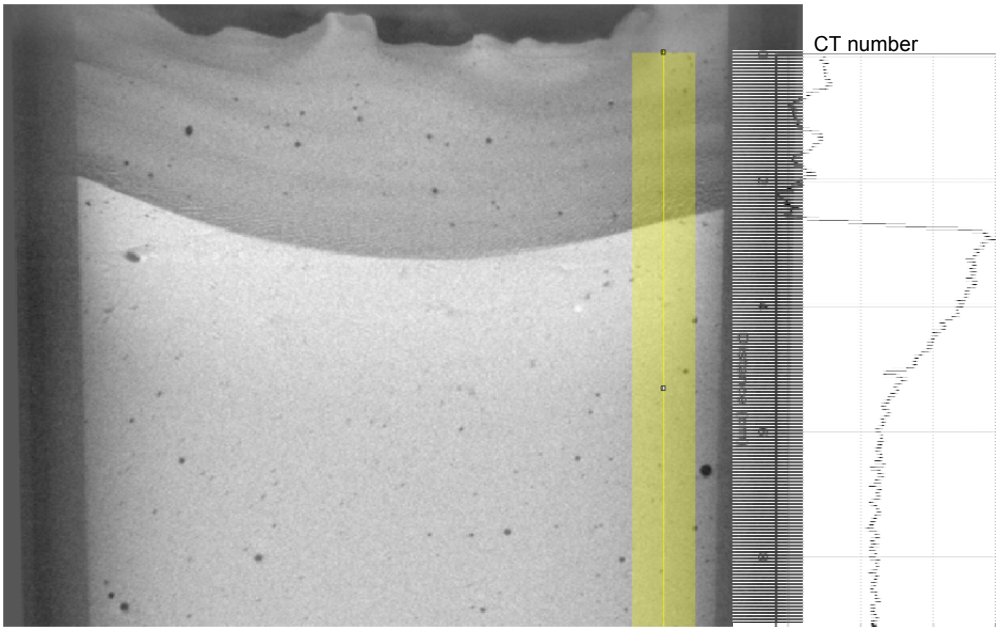

Figure 3.2 Cryogenic suction during ice/hydrate formation. The CT image shows a vertical slice of a 3D kaolinite specimen as the freezing front advances from the top. The CT number along with the vertical direction that corresponds to the highlighted line.

Cryogenic suction, water migration and ion exclusion during hydrate formation alter the physical properties of the sediment that surround the segregated hydrate. Therefore, it is not appropriate to use the properties of the normally consolidated sediments NCS in a two-component effective medium model: in fact, the stiffness, strength, and thermal conductivity of the sediments after hydrate formation is higher than for the normally consolidated sediments at the same burial depth or effective stress; on the other hand, the sediment hydraulic conductivity decreases with the reduction in void ratio. The electrical conductivity response of the sediment that surrounds the hydrate mass is complex and varies

in time: it decreases with the reduction in porosity, but it increases due to ion-exclusion; however, excess ions eventually diffuse away.

3.2 Impacts of lens on fundamental properties

Numerical simulations are conducted to estimate the physical properties of fine-grained hydrate-bearing sediments.

Conduction properties. Figure 3.3 compiles the simulation results of the thermal conductivities as a function of hydrate mass orientation θ. The effective thermal conductivity of the sediments with a single ellipse lens follows the equation below

$$K_T = K_0 \cos^2\theta + K_{90} \sin^2\theta \tag{3.1}$$

where K_T is the effective thermal conductivity, K_0 and K_{90} are the effective thermal conductivities when the lens is perpendicular and parallel to the thermal gradient respectively, and θ is the orientation of the hydrate mass. By contrast, the effective thermal conductivity of the sediments that contain crossed hydrate lenses is not sensitive to the lens orientation.

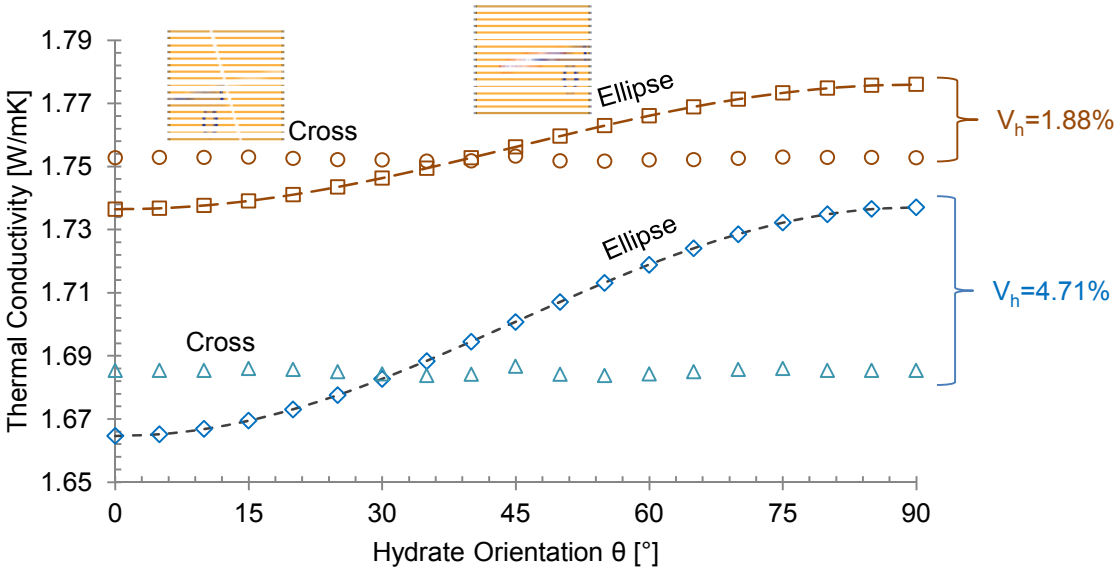

Figure 3.3 Effective thermal conductivity of hydrate-bearing fine-grained sediments as a function of hydrate mass orientation θ. Lines represent physical models; dots are numerical simulation results.

Results for thermal conductivity apply to electrical conductivity, magnetic permeability, and dielectric permittivity as well. The effect of hydrate lenses on effective media properties reflects the corresponding physical properties. For example, the hydraulic and electrical conductivities of hydrate are close to zero. Therefore, the cutoff effect of hydrate on the water flow and electric current is more significant than the effect on heat flow.

Small strain. This section analyzes the bulk modulus *B* due to its importance in wave propagation. It is common to use wave velocity profiles to estimate hydrate saturation rate (Chand et al., 2004; Ghosh et al., 2010; Lee and Collett, 2005; Waite et al., 2009). COMSOL is used to study the elastic properties of hydrate-bearing fine-grained sediments. The effective bulk modulus is the volume average of all the components in the effective medium. The bulk modulus increases with the hydrate saturation.

Figure 3.4 presents the negligible influence of hydrate mass orientation θ on the bulk modulus of hydrate-bearing fine-grained sediments. This is primarily due to the inherent isotropic stress boundary condition associated with bulk modulus. The influences of the hydrate fraction and the type of geometrical distribution are much more significant.

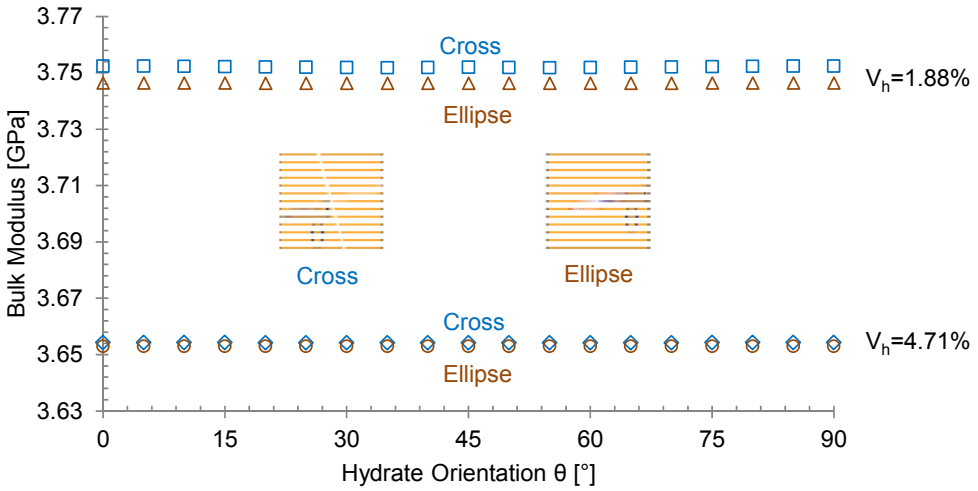

Figure 3.4 Effective bulk modulus of hydrate-bearing fine-grained sediments as a function of hydrate mass orientation θ. Lines represent physical models; dots are numerical simulation results.

Large strain. The strength analyses include two conditions, non-slip contact and frictional contact between hydrate lens and the sediments. The hydrate lens elements share the same nodes with the soil elements in non-slip contact simulations. This corresponds to when the hydrate is in growing or is stable. Interfaces between the hydrates and the sediments are

rough and jagged (See session 3.1). Therefore, there is unlikely to be slippage between the hydrates and sediment in the loading process. However, when the hydrate dissociates during gas production, the dissociation firstly occurs on the interface. Consequently, the contact between hydrates and sediments becomes slippery due to the presence of produced gasses. The characterization of the strength of the sediments then uses frictional contacts. The simulation uses a thin layer of material with a low friction angle (φ = 5°) to represent the frictional contact.

Figure 3.5 presents the displacement and in-plane shear stress field of the hydrate-bearing fine-grained sediments. The localized in-plane shear stress induces the later development of shear bands. When the interface is non-slip, the hydrate mass enhances the sediment strength by the inhibition of shear band formation. Therefore, two shear bands form around but do not cross the hydrate lens. However, when there is a frictional interface, one shear band develops along the interface. The shear band forms at a much lower vertical strain level in frictional conditions compared to the non-slip case.

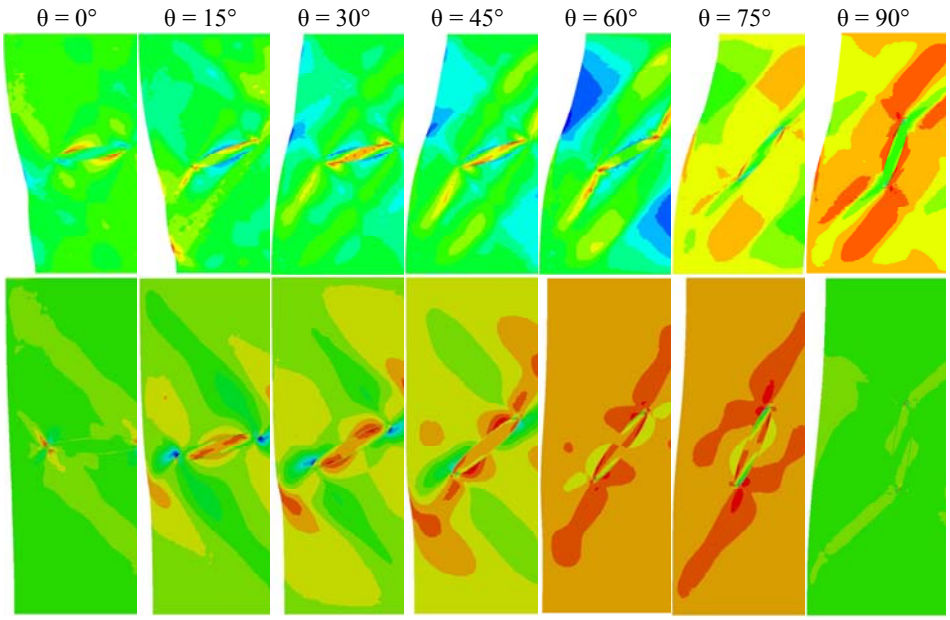

Figure 3.5 Fine-grained sediment with a single segregated hydrate lens subjected to shear. In-plane shear stress fields for various lens orientation θ. (a) Frictional hydrate-sediment interface, (b) Non-slip hydrate-sediment interface.

Figure 3.6 shows the simulation results of sediments that contain cross hydrate lenses. The hydrate lenses behave as reinforcements to the sediment. When the load transfers directly through the hydrate lenses (0°), the overall sediment strength reaches its peak. The influ-

ence of the interface strength is negligible in this condition. However, a slight tilt of the hydrate lenses can result in a significant strength decrease. The shear resistance of the overall sediment controls the load capacity, and the interface strength becomes critical as the angle of orientation θ increases. Shear stress localizes at the intersection of hydrate lenses in the slip interface condition. The hydrate yields and breaks when the shear force exceeds its strength. This could be an important failure mechanism when gas hydrate dissociates.

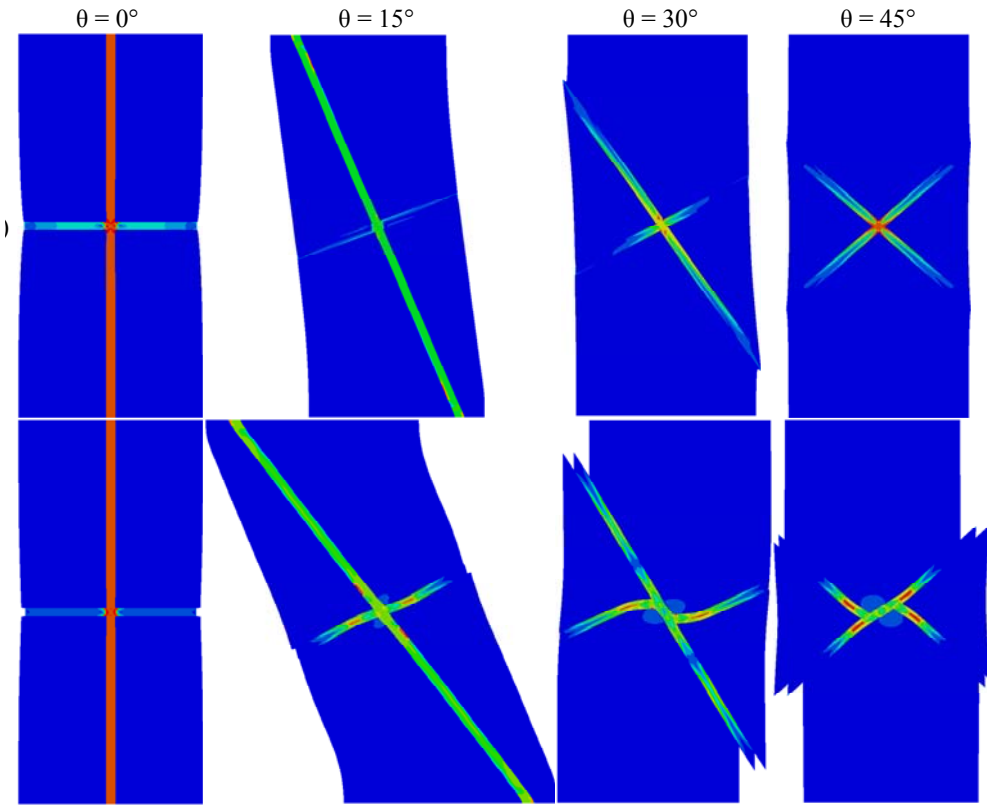

Figure 3.6 Fine-grained sediment with two normally-intersecting hydrate lenses at different orientation θ. (a) Frictional hydrate-sediment interface, (b) Non-slip hydrate-sediment interface.

Figure 3.7 summarizes the shear strength simulation results. The total strength of the sediments reaches the peak when the lenses direction is parallel or perpendicular to the load direction. This strength decreases as hydrate lenses tilt towards 45°. In addition, Figure 3.7 presents the strength of sediment prior to hydrate formation. The contribution of the consolidation effect to the strength of the sediments is dramatically higher than the contribution of the hydrate lens.

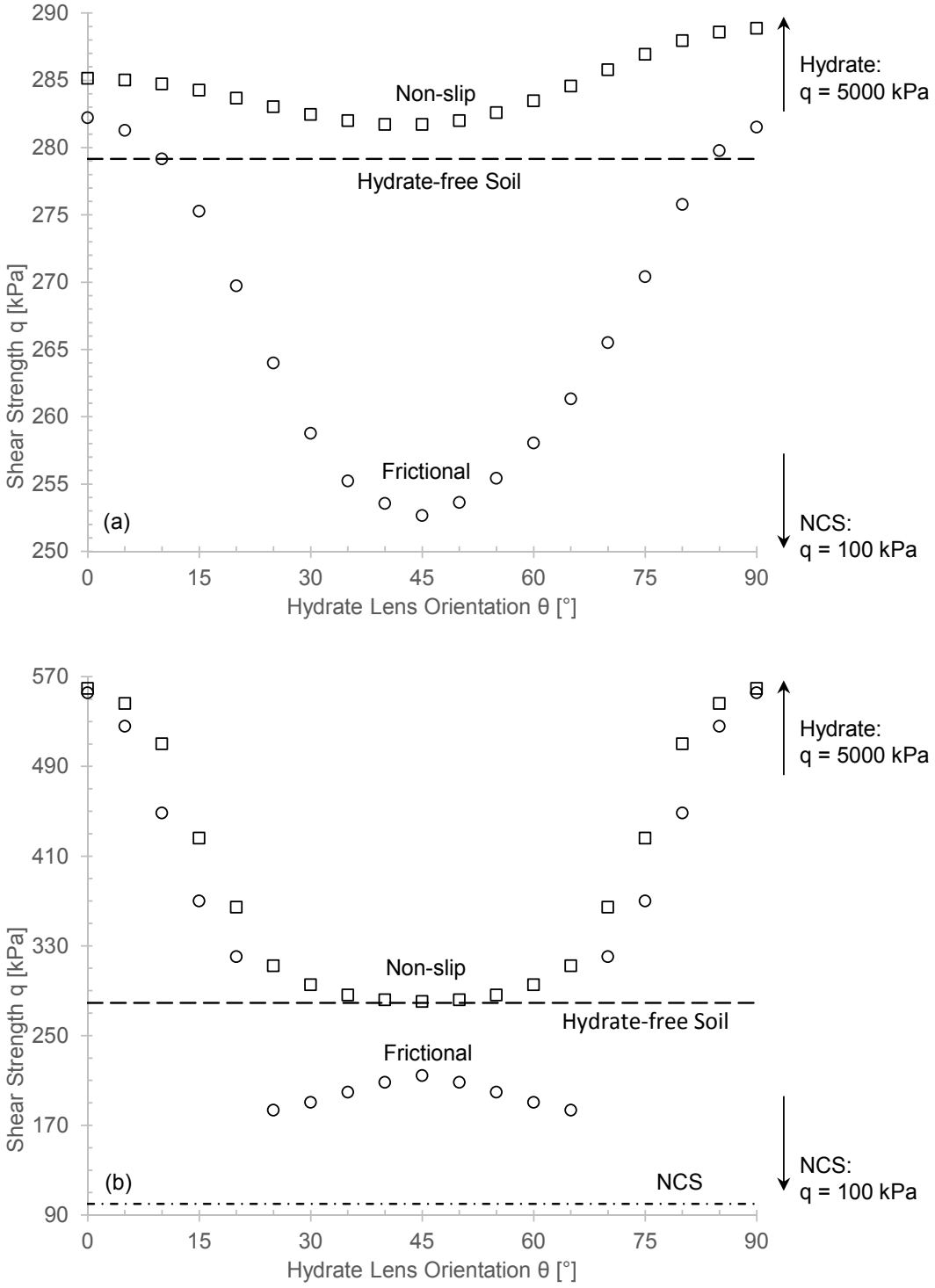

Figure 3.7 Shear strength of segregated-hydrate in fine-grained sediments with frictional and non-slip hydrate-sediment interface as a function of hydrate orientation θ. (a) Fine-grained sediment with a single segregated hydrate lens, (b) Fine-grained sediment with two normally-intersecting hydrate lenses.

Boundary effects. Boundary effects become significant when the assessment of strength and stiffness uses square specimens. Figures 3.8 presents the shear strength of the sediments with the frictional interface as a function of hydrate mass orientation. When the weak layer interconnects with the shear band in the soil, the soil strength dramatically decreases. The interconnection in a square specimen most effectively occurs when the title angle equals 30° and 60°. Consequently, the shear strength q exhibits two valleys correspondingly. However, the shear band that cuts the constant stress boundary at 30° yields less resistance in comparison to the shear band along the 60° weak line that crosses the predetermined displacement boundary. Therefore, the strength of the specimen at 30° is lower than at 60°.

The two valleys in the strength of the specimen are due to the boundary effect and do not represent the true large strain mechanical behavior of hydrate-bearing sediments. Therefore, laboratory tests should use long specimens to ensure that the shear band does not cross the displacement-controlled boundaries. Figure 3.8b demonstrates the location of shear bands and hydrate lens in a long specimen. It requires that the geometry satisfy

$$h > a + 2z = a + b\tan\theta \tag{3.2}$$

where a is the hydrate lens length, b is the specimen width/diameter, $\theta = 45° + \varphi/2$ and φ is the friction angle of the sediments. When the friction angle φ is 30° and $a = 0.6b$, the length of the specimen should be larger than 2.33 times of the specimen width/diameter. The simulation in this study uses a length to width ratio of 2.5.

(a) (b)

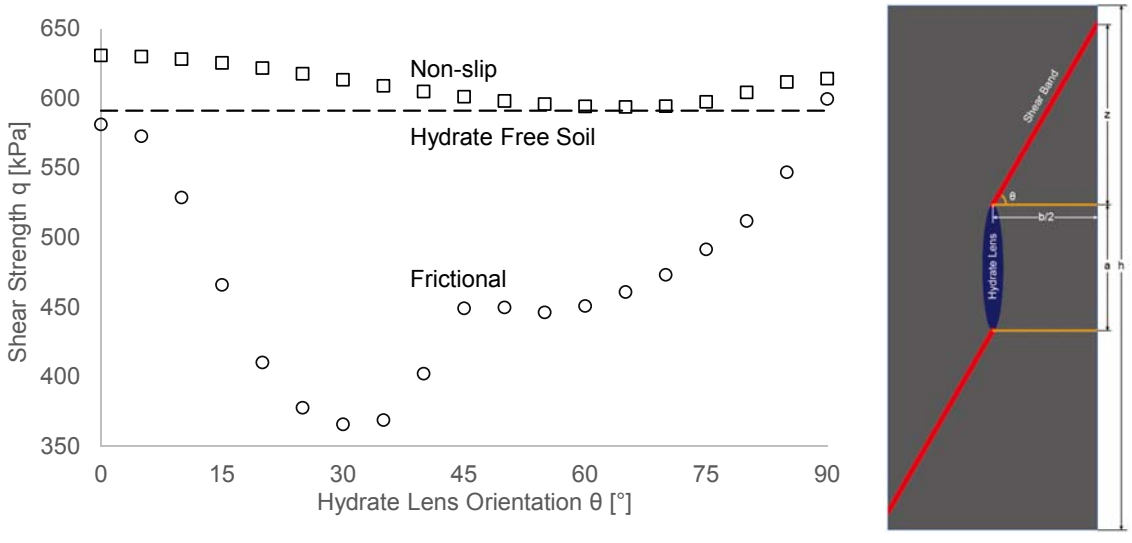

Figure 3.8 Boundary effect. (a) Lens orientation dependent shear strength. (b) The requirement on specimen length to eliminate boundary effects.

3.3 Laboratory measurement of the elastic and dynamic properties

THF is used as a proxy of hydrate formed in clayey sediments (i.e., kaolinite). Specimens are prepared by mixing THF, water, and kaolinite with the same mass ratios but different super-cooling temperatures. Resulted hydrates in kaolinite show different morphology and saturation (Figure 3.9).

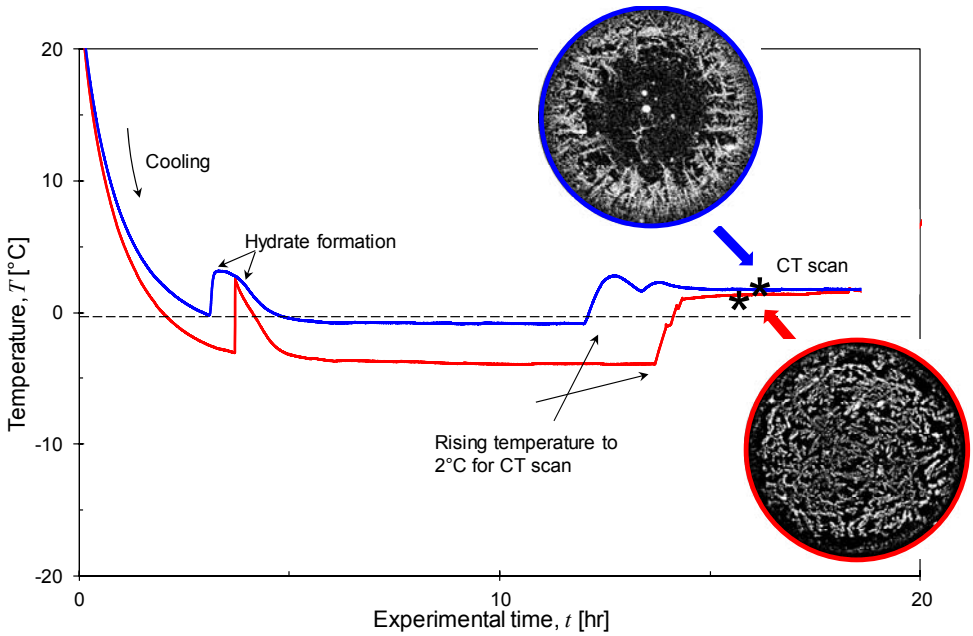

Figure 3.9 Temperature signatures and X-ray images of two specimens with an identical initial mass ratio of 100% stoichiometric solution and clay, i.e., 60:100 in this case.

Figure 3.10 shows the 3D CT images of hydrate in kaolinite sediments. Hydrate morphology and saturation vary with (THF, water, kaolinite) mass fractions and super-cooling temperature. Even for specimens with identical mass composition, final hydrate saturation and morphology are a difference depending on the supercooling temperature that governs the heat and mass transfer during hydrate formation.

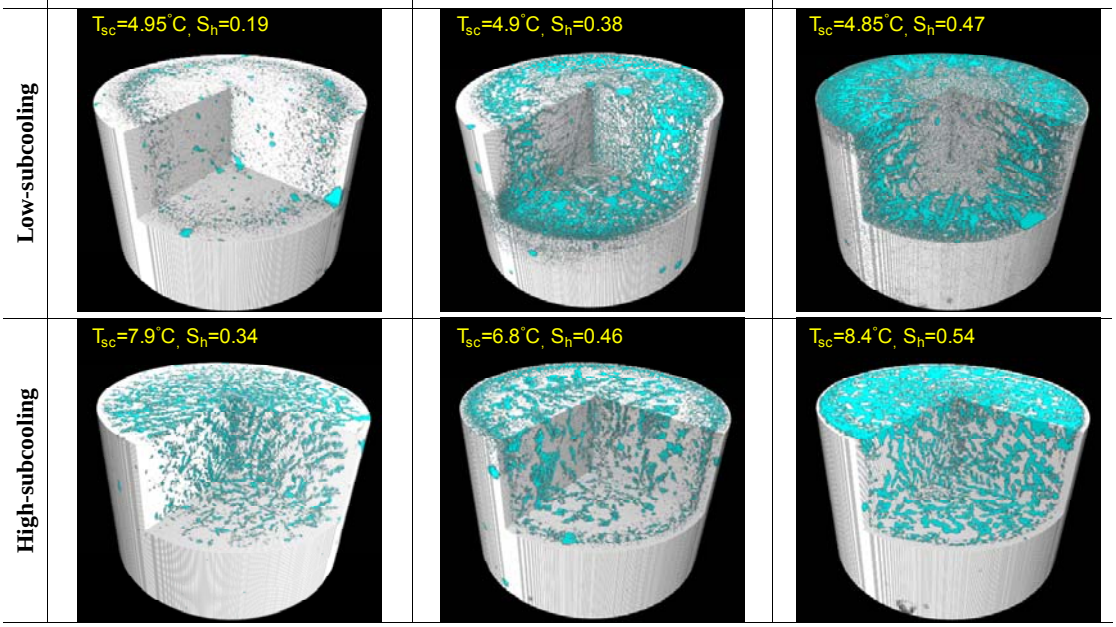

Figure 3.10 3D X-ray CT images of six hydrate-bearing specimens with different initial mass ratios and supercooling temperature (T_{sc}).

Elastic properties. Measured p- and s-wave velocities as a function of hydrate saturation are presented in Figure 3.11. With simultaneous measurement of p- and s-wave velocities, all elastic moduli (i.e., Young's, shear, constraint, and bulk moduli) of the hydrate-bearing sediments can be computed, as well as the Poisson's ratio. Although data are scattered, the self-consistent model can still capture the hydrate saturation dependent elastic properties for hydrate-bearing clayey sediments with a heterogeneous distribution of the hydrate.

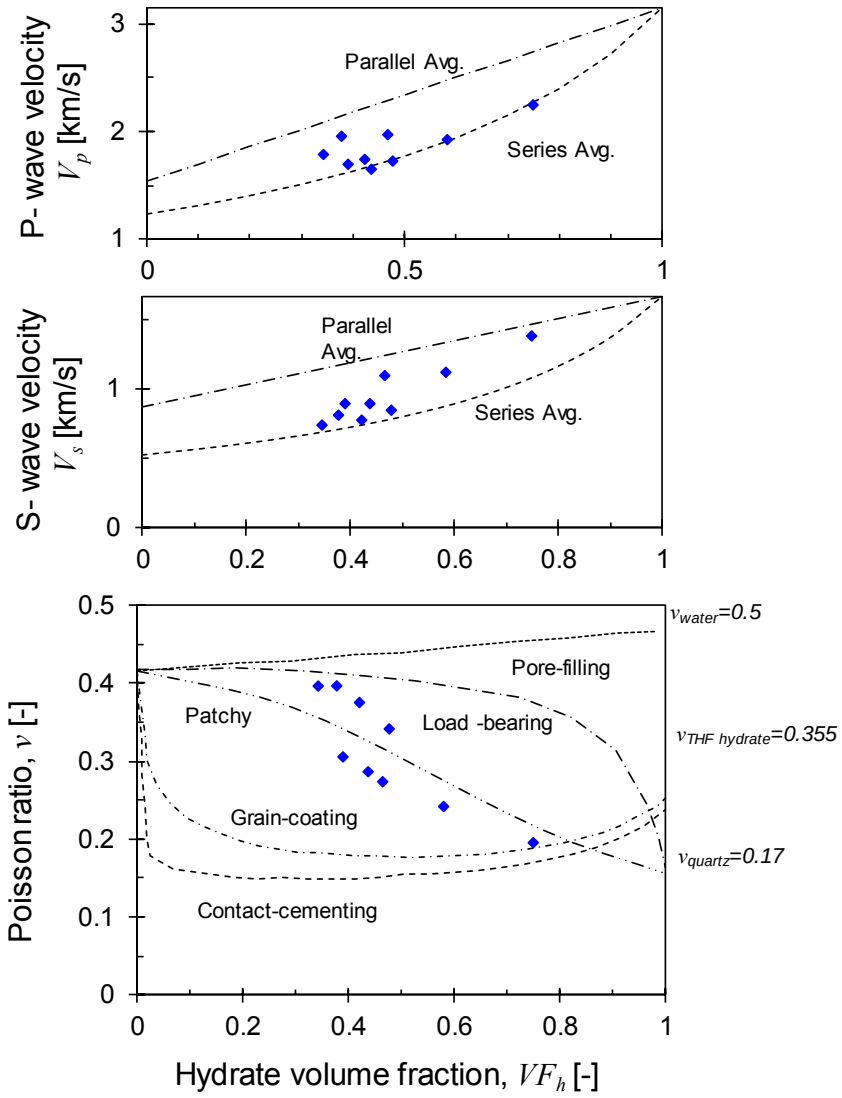

Figure 3.11 Elastic properties of THF hydrate-bearing sediments. (a) P-wave velocity versus hydrate saturation. (b) S-wave velocity versus hydrate saturation. (c) Poisson's ratio versus hydrate saturation. These elastic properties are not monotonically depending on hydrate saturation mainly due to random distribution and morphology of segregated hydrate lenses.

Dynamic properties. The presence of hydrate in the sediments makes the sediments stiffer, yet attenuates the wave more efficiently. Measured quality factor Q^{-1} values range between hydrate-bearing sediments and pure THF hydrate (reported in the literature).

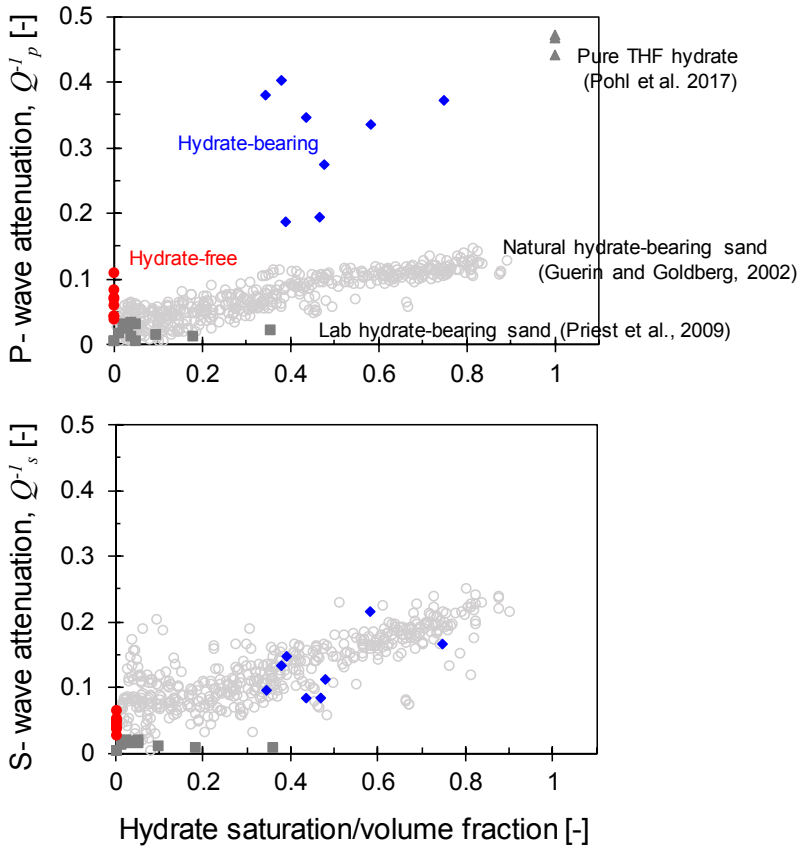

Figure 3.12 Measured quality factor Q^{-1} (i.e., damping) from both p- and s-waves in THF hydrate-bearing clayey sediments.

4. Gas production

4.1 Hydrate dissociation in clayey sediments – laboratory tests

CO2 hydrate dissociation generates massive gas driven fractures (Figure 4.1). Results of Tests 11 and 15-22 (Table 2.1 in Session 2.5) show the presence of both free water on the surface and gas within the fractures and cavities of the specimen. The surface water does not flow back into the specimen, despite the positive effects of gravity. Therefore, the fractures in the specimen cannot reach the surface after gas release. Following depressurization, fractures that previously housed hydrate now contain water released from hydrate dissociation. This change occurs when the pressure and temperature move away from the CO2 hydrate stability field.

The time-lapse images demonstrate the hydrate formation on the specimen surface, the lenses inside the specimen and the hollow gas hydrate structure that invades into the specimen, and the evolution of crack formation and development during hydrate dissociation.

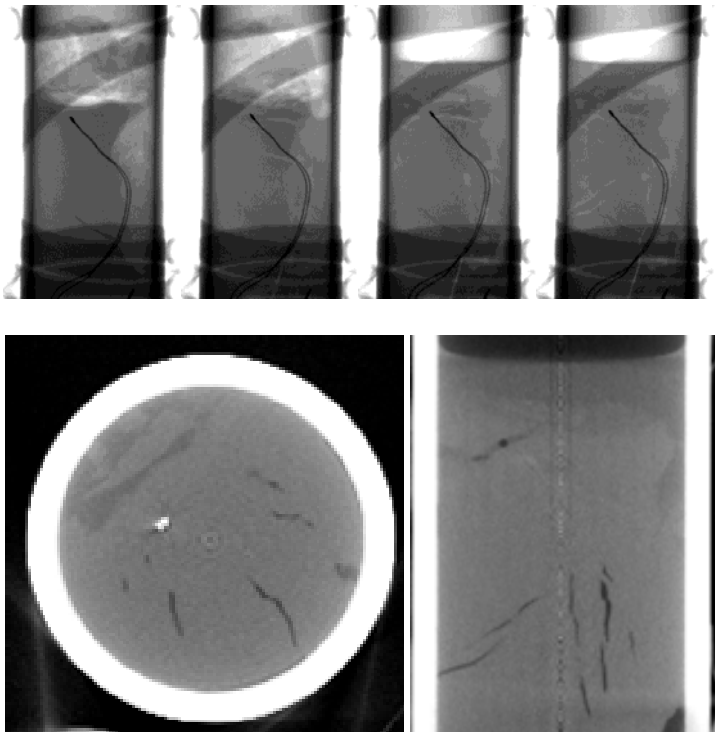

Figure 4.1 Hydrate dissociation developed by depressurization. (a) Projections; (b) Horizontal and vertical slices of CT gathered after dissociation.

4.2 Gas flow patterns

There are three boundaries that determine the flow behavior in sediments (Figure 4.2).

Boundary 1: when the effective stress σ' is larger than the characteristic capillary pressure C^*_{gw}, the fabric of the soil skeleton does not change due to the influence of the capillary pressure:

$$\sigma' = C^*_{gw} = \Gamma_{gw} \frac{4\cos\theta}{d^*}. \tag{4.1}$$

Boundary 2: when the difference between the gas and water pressure is larger than the characteristic capillary pressure of the sediment, gas can potentially invade into the pore space:

$$P_g - u_w = C^*_{gw}. \tag{4.2}$$

The unbalanced force between the water and gas transfers to the capillary tube, which is assumed to be rigid and has sufficient strength. However, the capillary tube is compressible and has strength limitations in reality. Therefore, the unbalanced forces can deform or even break the capillary tube.

Boundary 3: the soil skeleton functions as the capillary tube and the effective stress caps the strength. When the difference between the gas and water pressure is larger than the effective stress, it is potential for cracks to form in the sediment (Shin and Santamarina, 2011).

$$P_g - u_w = \sigma'. \tag{4.3}$$

The pressure difference between gas and water, effective stress and characteristic capillary pressure determine the macro-scale behaviors of the sediment. Figure 4.2 divides the entire σ'-(Pg-uw) field into six different zones based on the three boundaries:

- Zone *N1*: P_g-u_w <σ' < C^*_{gw}. The effective stress limits gas flow.
- Zone *N2*: P_g-u_w <C^*_{gw} < σ'. The characteristic capillary pressure limits gas flow.
- Zone *Y1*: σ' <P_g-u_w <C^*_{gw}. Gas does not have the capability to invade into sediment pores due to the water surface tension. Gas flow only occurs through gas-driven fractures (Shin and Santamarina 2011).
- Zone *Y2*: C^*_{gw} <P_g-u_w <σ'. Gas flow only occurs through the connected pores. The soil fabric does not change due to gas flow.
- Zone *Y3*: σ' <C^*_{gw} <P_g-u_w. Gas flow is primarily through the gas-driven fractures. Dynamic gas flow can invade into sediment pores simultaneously.

- Zone *Y4*: C^*_{gw} <σ' <P_g-u_w. Gas flow is typically through the connected pores. Meanwhile, a dynamic gas flow can potentially create gas-driven fractures by the effect of dragging force, which dramatically accelerates the gas flow rate.

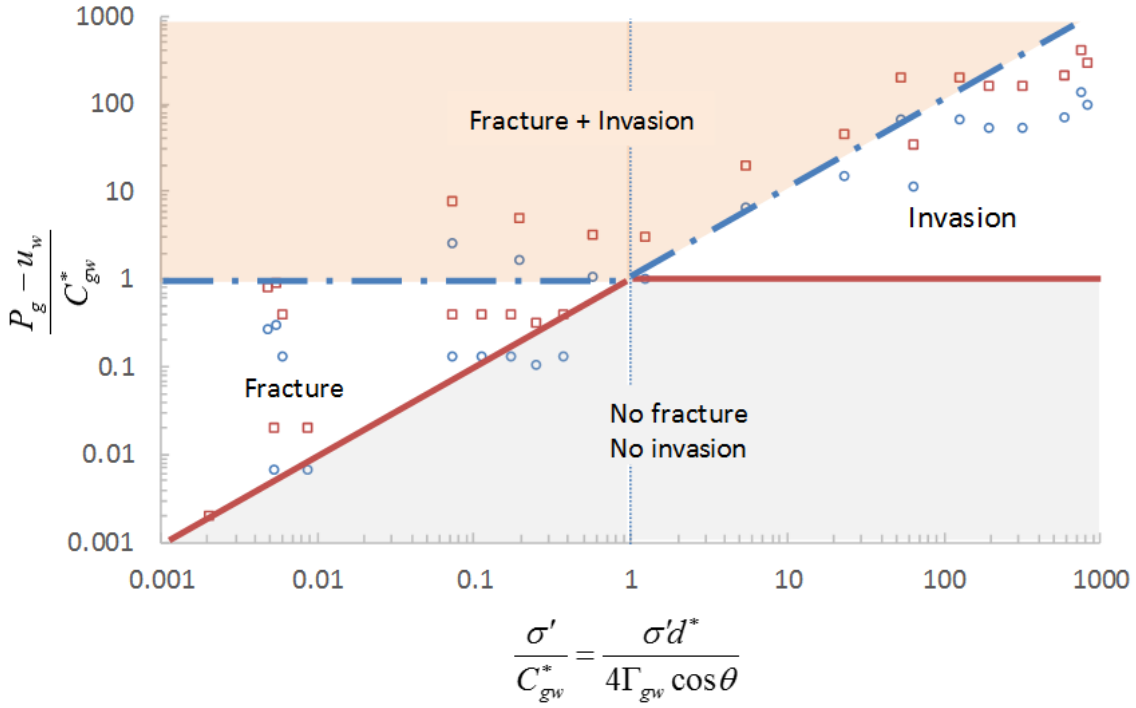

Figure 4.2 Balance between the effective stress σ', characteristic capillary pressure C^*_{gw} and the pressure difference between the gas and water P_g-u_w. Different regions inferred from equilibrium conditions. Dots represent different site conditions. We assume the pressure difference for all the sites is either 1MPa (○) or 3MPa (□).

4.3 Gas production from fine-grained sediments

There are generally three methods for gas production from gas hydrate-bearing sediments: depressurization, thermal stimulation, and chemical stimulation including the CO_2-CH_4 replacement. This section discusses the potential of each method in fine-grained sediments and notes the importance of the capillary effect to gas production in fine-grained sediments.

This work does not consider the capillary effect on the gas hydrate phase boundary in gas production, as hydrates with the highest curvature dissociate first, and then further hydrate dissociation consumes the residual bulk hydrate at the bulk hydrate phase boundary. Capillary pressure inhibits hydrate dissociation. The depressurization method demands a

lower water pressure than the phase boundary pressure to dissociate the residual hydrate. By contrast, the thermal stimulation technique requires a higher temperature at this point to destabilize the residual hydrate. The gas pressure around the hydrate crystal is higher than the water pressure. The gas pressure maintains the stability of the residual hydrate before the pressure difference between water and gas exceeds the characteristic capillary pressure.

Depressurization. The most successful gas production technique from gas hydrate sandy reservoirs is depressurization (Dallimore et al., 2012; Hunter et al., 2011; Yamamoto et al., 2014). However, depressurization-driven gas production in fine-grained sediments has difficulties in (i) gas flow, which does not occur until the pressure difference between the gas and water exceeds the barrier pressure difference, (ii) effective stress increases, which induces sediment consolidation, accompanied by a reduction in the pore size and hydraulic conductivity, (iii) well production challenges including sediment volumes contract as the effective stress increases and cause subsidence and potential good stability issues, (iv) geometric restrictions prevent gas driven fractures in these conditions, and (v) flow rate limitations, as the characteristic capillary pressure reaches 1MPa when the pore size decreases to 1.5μm, and 5MPa for 0.3μm pores; well production costs increase as the particle size decreases, due to the lower hydraulic conductivity in these conditions regardless of the capillary barrier.

Thermal stimulation. Water and sediments consume the majority of the injected thermal heat in production wells, with minimal heat consumed by gas hydrates. Therefore, pure thermal stimulation is uneconomical for this reason (Moridis, 2008; Moridis et al., 2007). The barrier pressure difference determines the minimum required pressure increase to enable gas production. The slope of the hydrate phase boundary increases with the temperature increase. Therefore, the same amount of pressure increase corresponds to a smaller temperature increase at higher temperatures. This indicates that the thermal stimulation method is more efficient at high-temperature sites.

When the PT trajectory deviates from the phase boundary, the gas hydrates completely dissociate. The slope of the pressure increase versus the temperature increase is significantly flatter than that of the hydrate phase boundary. Therefore, further thermal stimulation that aims to increase the gas pressure becomes inefficient.

Chemical stimulation and replacement. Chemical stimulation and CO_2-CH_4 replacement both rely on the transport of molecules to the reaction front. However, the small pores and

high specific surface in fine-grained sediments implicate inefficient substance migration. The Péclet number (P_e) is approximately proportional to the cubed grain diameter. The contribution of advection to the process of substance transfer in porous media decreases dramatically as the grain size decreases. When P_e <1, diffusion dominates the transfer and decreases the transfer speed. Consequently, the chemical transfer in fine-grained sediments is time intensive and uneconomical.

A number of hydrate dissociation experiments in water with chemicals dissolved exhibit the freshening effect (Østergaard et al., 2002). Gas hydrate dissociation releases fresh water into the environment. The freshwater dilutes all the dissolved components and reduces their concentration. This triggers the movement of the shifted gas hydrate phase boundary back to the bulk gas hydrate phase boundary as gas production continues. Similarly, the freshening effect can also reduce the concentration of any injected chemicals as the gas hydrate dissociates. The chemical stimulation methods detailed above do not permit continuous gas production.

Surface mining in shallow marine sediments. Shallow hydrate-bearing fine-grained sediments are found in Hydrate Ridge (Hovland et al., 1995), the Gulf of Mexico (Pflaum et al., 1986), the Sea of Okhotsk (Luan et al., 2008), and offshore India (Kumar et al., 2014). Shallow marine fine-grained sediments have the potential to accumulate large quantities of hydrates. Firstly, the effective stress in shallow sediments is low, yet the characteristic capillary pressure is high. These circumstances enable large quantities of gas to form cavities. Hydrate forms when these same gasses combine with water. Secondly, the low effective stress places fewer limitations on gas hydrate formation in comparison to deep fine-grained sediments. Thirdly, the water supply for gas hydrate formation could potentially come from the sea. By contrast, gas hydrate formation in deep sediments extracts water from the consolidated sediments, a process that requires a large degree of temperature depression. Therefore, shallow fine-grained marine sediments commonly contain large hydrate crystals (Suess et al., 2001).

The proposed concept of gas production is the surface mining in shallow marine sediments. The circulation of warm water from the sea surface increases the sediment temperature. Gas hydrate in the sediments dissociates upon heat absorption. The increased gas pressure then overcomes the barrier pressure difference to create gas-driven fractures or drives gas flow through the pores. Membranes or umbrellas approximately the size of a football field then collect the gas or even gas hydrate.

The surface mining in shallow marine sediments applies to all sediment types. The characteristic capillary pressure is low in coarse-grained sediments due to the large pore size.

Therefore, gas production occurs through the connected pores. The low effective stress in shallow fine-grained sediments allows low gas pressures to create gas-driven fractures, which can produce a number of gas flow paths.

Hydrate formation uses the gas released from the sediments. Methane bubbles from this release rise due to buoyancy. An upside-down container on the sea floor collects the bubbles. Stirring within the container then accelerates the hydrate formation process. The hydrate could then be harvested in the solid form.

Fine-grained sediments usually possess a high compression index. The effective stress in shallow marine sediments less than 10 meters below the sea floor is usually not larger than 100kPa. However, the increase in effective stress due to depressurization can be up to 30,000kPa if the PT of the sites is deep within the hydrate phase boundary. The same amount of effective stress change in kaolinite results in a 50% volume contraction, a pore size reduction from 1000nm to 100nm, and a change in the void ratio from 1.38 to 0.2 (Chong and Santamarina, 2016). The characteristic capillary pressure is inversely proportional to the pore size. Therefore, the barrier pressure difference increases up to 10 times of the original. The effective stress increase develops in the sediments during well gas production, regardless of the method used. By contrast to depressurization, gas pressure increases due to thermal stimulation do not necessarily increase the effective stress. When we use surface mining techniques in shallow marine sediments, the increased gas pressure can generate gas-driven fractures without an increase in the effective stress. Therefore, the pore size and hydraulic conductivity do not decrease while gas production occurs.

5. Implications

5.1 Maximum recoverable gas

Gas reservoirs in hydrate-bearing sediments can be classified as (Moridis, 2008):

- Class 1: high hydrate saturation layer on top of a layer with free gas and water.
- Class 2: similar to class 1 but there is no free gas beneath (only mobile water).
- Class 3: absence of free fluids underneath (semi-confined aquifer).
- Class 4: low hydrate saturation (< 10%), and lack of confining stratum.

Class 1 reservoirs are most desirable because they are next to the phase boundary and a low energy input is required for dissociation. Class 4 is least desirable because they lack confinement and can lead to very low recovery efficiency.

Sandy deposits are currently preferred because of their high permeability and low compressibility. Reservoirs that are considered to be commercially feasible given today's state of the art are listed in Table 5.1.

Table 5.1 Selected reservoirs gas volume estimation.

Location	Gas estimation [m^3]	Reference
Mallik (Canada)	3 109 to 4 109	Moridis, 2002
The Gulf of Mexico	6 1014	BOEM report 2012
Mount Elbert (Alaska)	4 109	BOEM report 2012
Atlantic coast USA	6 1014	BOEM report 2012
Pacific coast USA	2.3 1014	BOEM report 2012
Ulleung Basin (Korea)	1015 to 1018	Moridis, 2013
Nankai Trough(Japan)	5.6 1011	Fujii et al 2013
ShenhuArea (China)	1.6 109	Wu et al. 2010
Krishna-Godavari basin (India)	9.8 108 to 5.6 109	Shankar and Riedel 2011

Analytical solution. Consider a stable hydrate-bearing sediment under high water pressure and low temperature. The reservoir is subjected to depressurization at the well. Gas production starts as soon as the pressure falls outside stability conditions. Eventually, steady state flow and pressure conditions are reached for a given well pressure u_w, the dissociation front stops advancing and hydrate dissociation ends. The distance from the well to the ultimate position of the dissociation boundary is the terminal radius r^* and defines the size of the produced zone; the fluid pressure at r^* is the pressure on the phase boundary u^* for the reservoir temperature. This boundary defines two zones in the reservoir at the end of

dissociation and under steady state flow conditions. The inner zone $r \le r^*$- that is characterized by the sediment permeability k_{sed} [m/s] (without hydrates but with partial water-gas saturation), the outer zone $r \ge r^*$ where hydrate-bearing sediment has permeability k_{hbs} [m/s]. The water pressure in the far field is u_{far}. Figure 5.1 summarizes the boundary conditions for the three cases analyzed next: radial flow in a homogeneous formation or a strata-bound reservoir with either a vertical well normal to the reservoir or a horizontal well within it.

Laplace's equation in spherical coordinates is written as

$$\nabla^2 u = \frac{1}{r^2}\frac{\partial}{\partial r}\left(r^2 \frac{\partial u}{\partial r}\right) + \frac{1}{r^2 \sin\theta}\left(\sin\theta \frac{\partial u}{\partial \theta}\right) + \frac{1}{r^2 \sin^2\theta}\frac{\partial^2 u}{\partial \xi^2} = 0\,, \tag{5.1}$$

where the azimuthal angle θ, the polar angle ξ, and the radius r define the location of any point in space. Tangential derivatives to equipotential lines vanish in radial flow, and the equation simplifies to

$$\nabla^2 u = \frac{1}{r^2}\frac{\partial}{\partial r}\left(r^2 \frac{\partial u}{\partial r}\right) = 0\,. \tag{5.2}$$

If fluid pressures u_1 and u_2 are known at radial distances r_1 and r_2, then the pressure field u_r is

$$u_r = u_1 + (u_2 - u_1)\left(\frac{r_1 - r}{r_1 - r_2}\right)\frac{r_2}{r}\,. \tag{5.3}$$

The flow rate q [m^3/s] can be computed from the flux across a sphere of area $4\pi r^2$ when the Darcy velocity is $(k/\gamma)\partial u/\partial r$:

$$q = -4\pi r^2 \frac{k}{\gamma_w}\frac{\partial u_r}{\partial r} = 4\pi \frac{k}{\gamma_w}\frac{u_2 - u_1}{\frac{1}{r_1} - \frac{1}{r_2}}\,. \tag{5.4}$$

Also, $q_{sed} = q_{hbs}$ at $r = r^*$ under steady state. Then, the terminal radius of the dissociation front r^* can be expressed as ($r_{far} >> r^*$):

$$r^* = r_w\left(1 + \frac{k_{sed}}{k_{hbs}}\frac{u^* - u_w}{u_{far} - u^*}\right). \tag{5.5}$$

General Description	Reservoir Characteristics
Homogeneous (*spherical radial flow*)	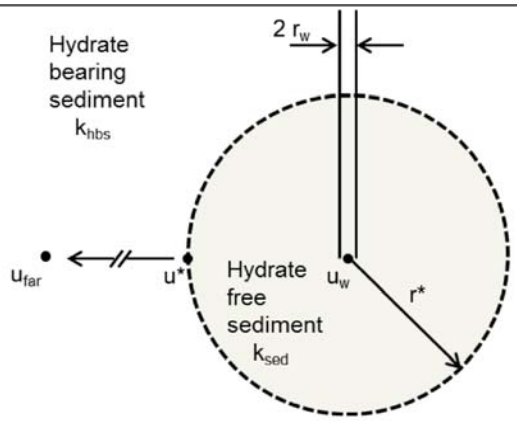
Strata-bound reservoir with leak-in Vertical well (*axisymmetric radial flow*)	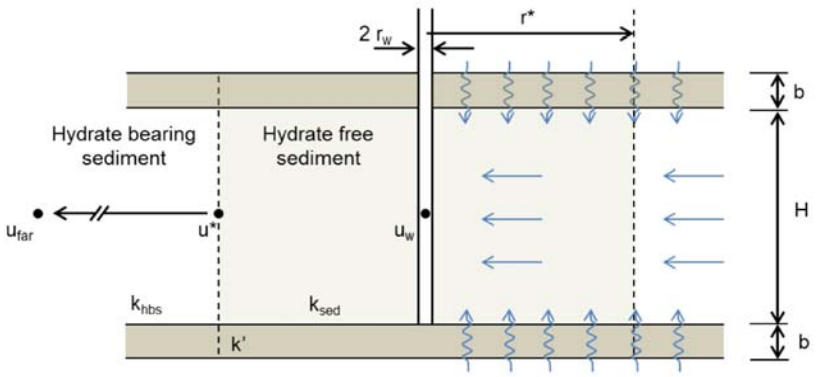
Strata-bound reservoir with leak-in Horizontal well (*parallel flow lines*)	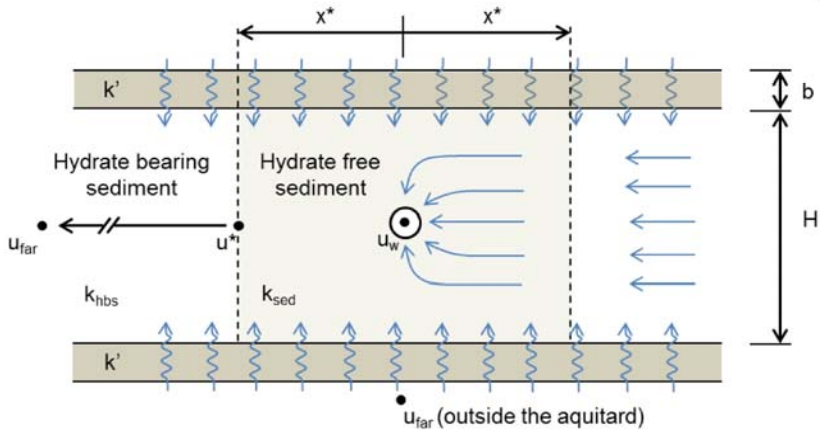

Figure 5.1 Reservoir characteristics and flow conditions (Terzariol et al., 2017). Well radius r_w in hydrate-bearing sediment layer thickness H and permeability k_{hyd} before dissociation and k_{sed} after dissociation. Aquitard permeability $k^{'}$ and thickness b. Fluid pressure at the well u_w, at the phase boundary u^* and in the far field u_{far}. Terminal size of the dissociation front in radial r^* or parallel x^* flow.

5.2 Sediment-well interaction

A fully coupled hydro-mechanical analysis is conducted to explore the consequences of depressurization. The complete length of the well is modeled to properly study the interaction between the sediment and the well. Special considerations related to the constitutive models used to represent salient processes are described first. These models are implemented in the multi-dimensional FEM simulator Geo-COUS (Geo-COUpled Simulator) specifically developed to investigate coupled phenomena in granular and/or porous media subjected to multi-phase flow.

Interface element. The axisymmetric finite element model consists of 8-node displacement and 4-node fluid pressure continuum elements. Thin hydro-mechanical interfacial elements are used to model the sediment–casing interface (6-node displacement and 4-node fluid pressure axisymmetric elements, modified from (Segura and Carol, 2008)). They have infinite transverse hydraulic conductivity, zero longitudinal conductivity, and quasi-infinite normal stiffness. The mobilized shear resistance τ is assumed elasto-plastic in terms of the relative shear displacement δ:

$$\tau = k_s \delta \quad for\, \delta \le \delta_y \,, \tag{5.6a}$$

$$\tau_{ult} = \sigma_r^{'} \tan\phi \quad for\, \delta > \delta_y \,, \tag{5.6b}$$

where δ_y is the yield displacement for sediment-wall shear; the ultimate shear strength τ_{ult} of the interface is proportional to the normal effective stress in the radial direction σ'_r and the sediment-casing friction angle ϕ (Coulomb model). The interface shear stiffness k_s increases as the normal effective stress increases. We capture this response by making $k_s = \tau_{ult}/\delta_y$. Then, the bilinear elasto-plastic shear response is completely defined by δ_y and ϕ.

Field case. The simulated field case represents conditions relevant to known hydrate accumulations in marine sediments that have been considered for production. The 156-m-long well is modeled as a constant diameter pipe (d =127mm, wall thickness 27mm). The hypothetical production horizon rests between 140 and 155mbsf (typically in Ulleung basin); thus, a 15-m-long production screen is modeled between z =140 and 155mbsf (Figure 5.2). A depressurization of Δu = −6MPa is gradually imposed (24hr ramp up) and kept constant thereafter. The simulation domain extends to a radial distance of 600m away from the well and to a depth of 300mbsf.

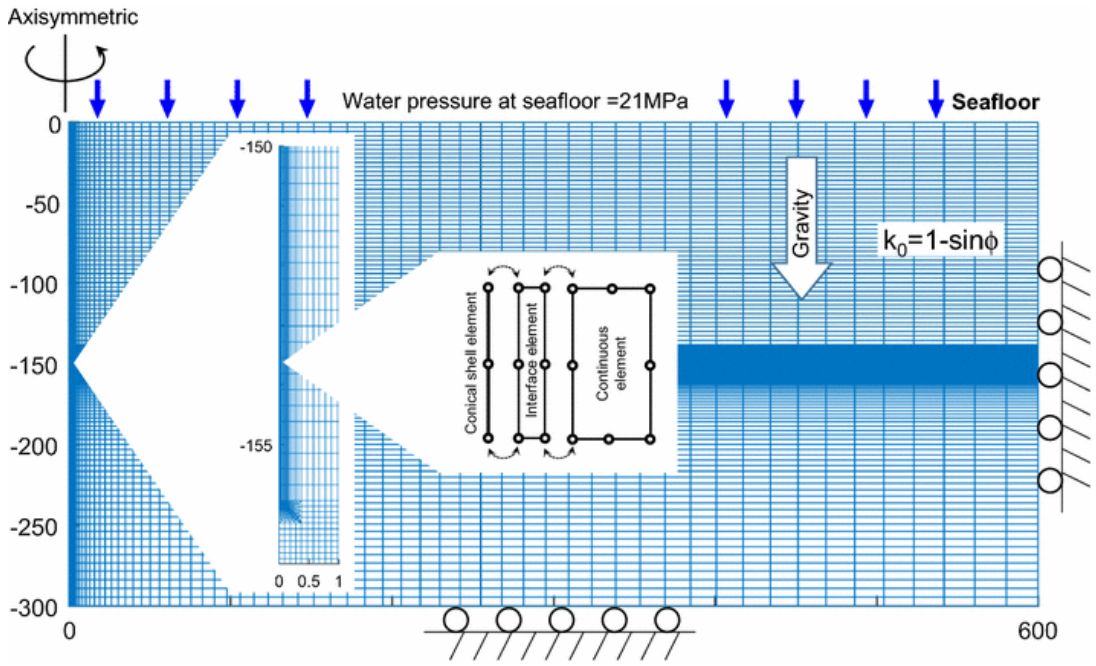

Figure 5.2 Numerical model: boundary conditions, initial conditions, and model geometry. Successive zoom-ins show the higher discretization within the production horizon and details at the sediment–well interface.

Compressibility-conductivity in the hydro-mechanical coupling. The coupled hydro-mechanical FEM model exposes the complex nature of sediment–well interaction during depressurization. In particular, the rapid pressure recovery away from the well is due in part to geometric effects (Laplacian), yet it is exacerbated by changes in permeability associated with compaction. Strong hydro-mechanical coupling between fluid pressure, effective stress, void ratio and permeability $u–\sigma'–e–k_u–\sigma'–e–k$ should be expected for clayey sediments as they are more compressible (higher C_c coefficient) and their permeability is more susceptible to changes in the void ratio (higher b-exponent).

Results in Figure 5.3 show that a higher b-exponent (at the same compressibility C_c) results in a narrower depressurization field, lower settlements and lower axial forces in the casing. In particular, the assumption of a constant hydraulic conductivity k (i.e., b =0) could lead to a gross overestimation of the axial force in the casing.

The formation of a compact sediment shell around the screen/pack in more compressible sediments (higher C_c and b-exponent) can have a prevalent effect on the system response and may lead to a counterintuitive response as shown in Figure 5.4: Compared to the low plasticity clay, the more compressible "high plasticity" clay develops a tighter sediment shell around the screen/pack, pressure recovers closer to the well, the vertical settlement is smaller in the more compressible sediment, and a lower axial load builds on the casing

(parameters in Table 5.2a—Note: Differences in friction angle can justify a ratio in peak loads of ~0.7 between the two cases).

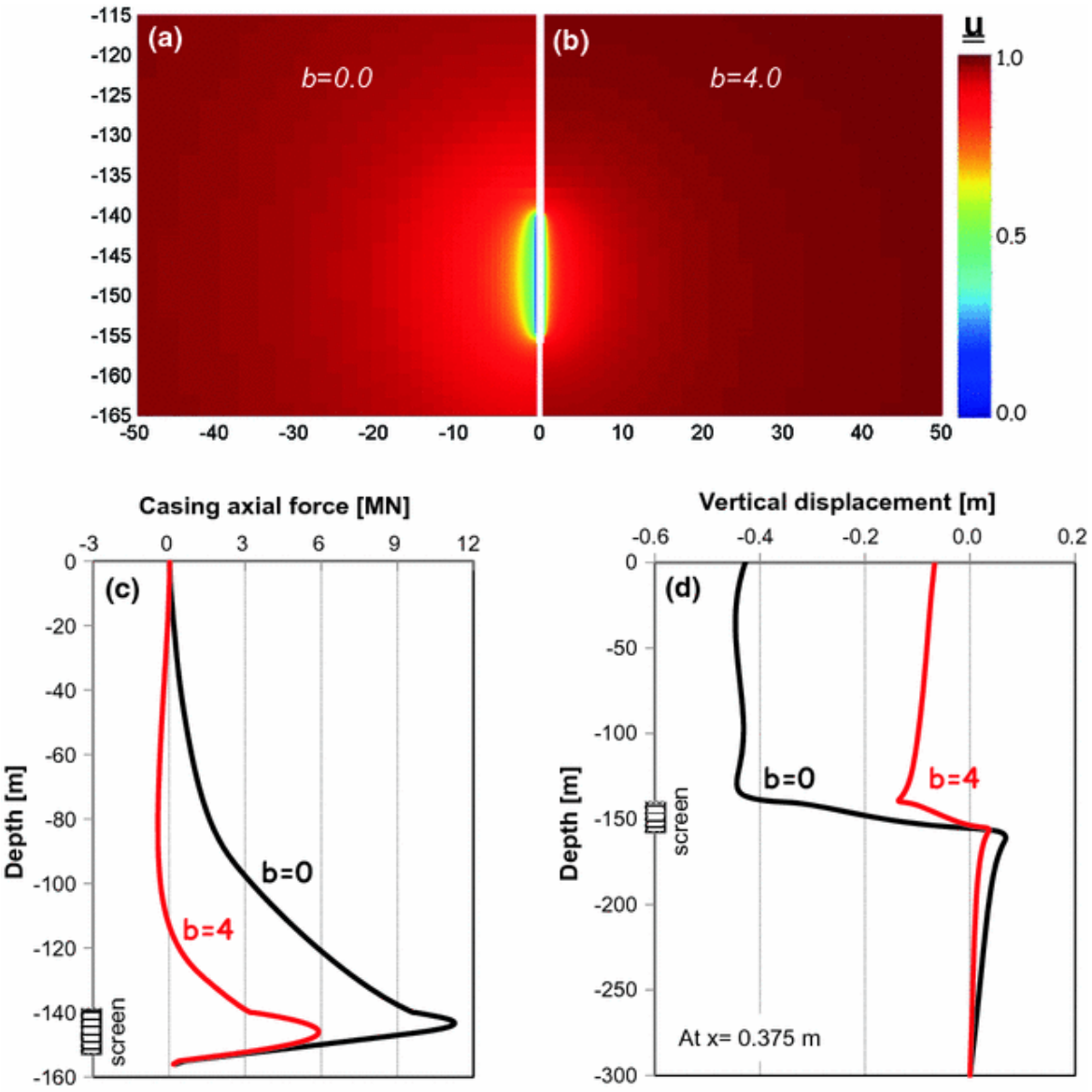

Figure 5.3 Hydro-mechanical coupling: stress-dependent permeability. Case: low plasticity clayey sediment with either constant permeability $b = 0$ or void ratio-dependent permeability $b = 4$. (a, b) Normalized fluid pressure $\underline{u} = (u - u_{well})/(u_{far} - u_{well})$. (c) Axial force distribution along the casing (negative = tension). (d) Vertical displacement measured at a radial distance x =0.375m.

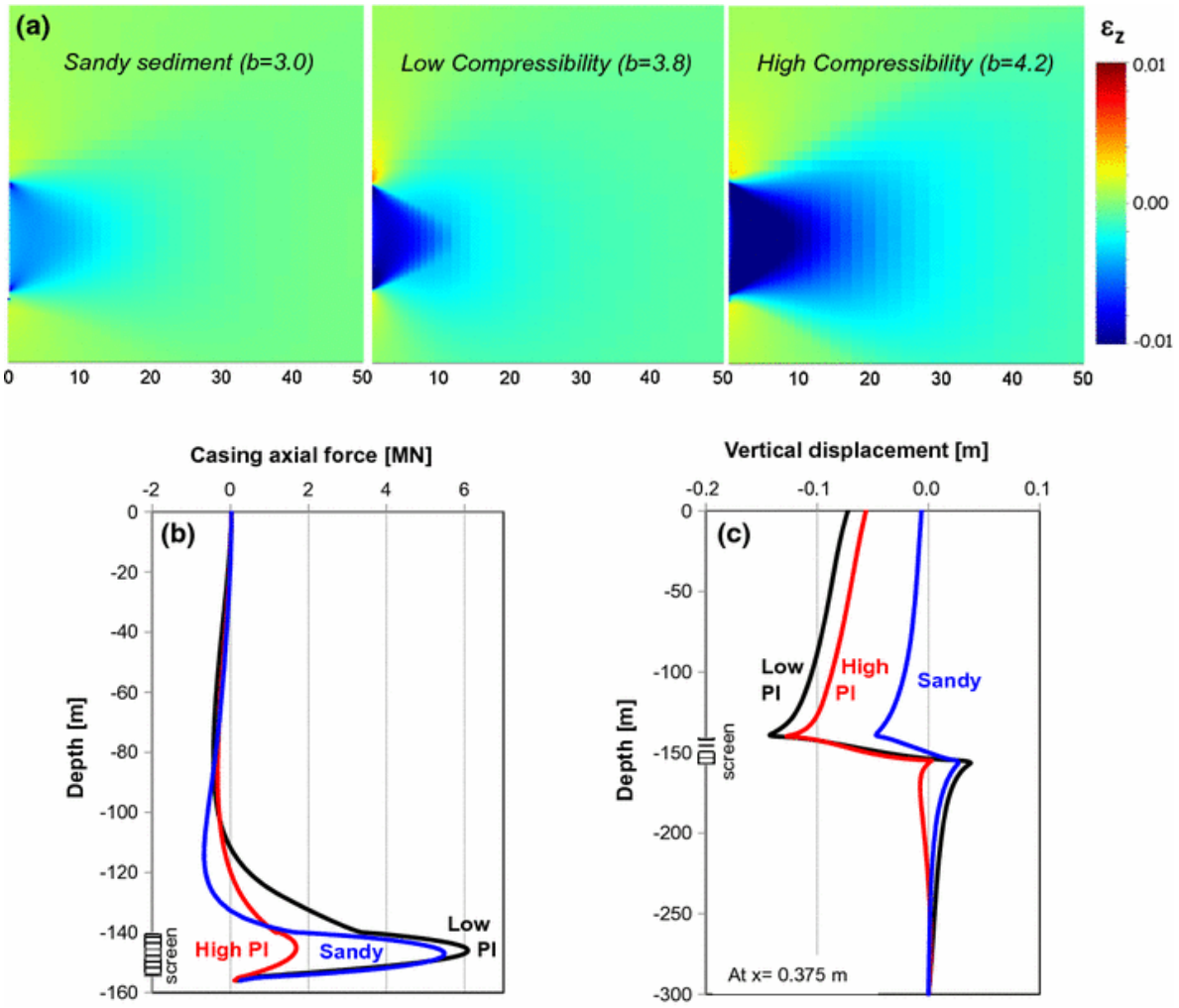

Figure 5.4 Effect of sediment compressibility and void ratio-dependent permeability. Cases: sandy sediment, low and high plasticity clayey sediments (All parameters in Table 5.2a). (a) Vertical strain. (b) Axial force distribution along the casing (negative = tension). (c) Vertical displacement measured at a radial distance x =0.375m.

Settlement. The settlement experienced by the production horizon and the settlement that reaches the seafloor are surprisingly similar in the four sediments studied here (Table 5.2b). This result highlights the tradeoff between high compressibility (high strains) and high void ratio-dependent permeability (smaller affected volume). For comparison, Table 5.2 includes the 1D settlement that the 15-m-thick layer between 140 and 155mbsf would experience if subjected to a homogeneous depressurization of Δu =6MPa: computed 1D settlements do scale with compressibility C_c and are more than an order of magnitude larger than the actual settlement computed using a formal analysis of hydro-mechanical coupling in well–sediment interaction.

Table 5.2 Selected sediments. (a) Constitutive parameters. (b) Layer compaction for 1D conditions versus computed settlement.

Modified Cam-Clay - associated flow rule		Plastic clayey sediment	Low IP clay-ey sediment	Diatoma-ceous sed-iment	Sandy sediment
a. Constitutive model					
Frictional strength	ϕ	14°	22°	27°	33°
Permeability	e_{ref}	1.0	1.0	1.0	1.0
	k_{ref}	10^{-10} cm/s	10^{-7} cm/s	10^{-9} cm/s	10^{-2} cm/s
	b	4.2	3.8	6	3.0
Compressibility	e_{1kPa}	4.8	1.7	4	0.8
	C_c	1.4	0.4	0.8	0.1
	e_L	4.0	1.4	3.6	0.7
	e_H	0.1	0.2	0.3	0.4
b. Layer compaction and settlement					
1D compaction					
Production layer compaction (m)		4.39	1.77	3.89	0.50
Wellbore production analysis					
Seabed settlement (cm)		5.6	7.2	7.8	0.6
Production layer compaction (cm)		13.0	16.6	18.6	7.0

6. Summary and Conclusions

This project increased the knowledge base of hydrate formation and dissociation in fine-grained sediments, developed laboratory techniques to emulate natural hydrate formation in fine-grained sediments, predicted the physical properties of hydrate-bearing fine-grained sediments using experimental, numerical, and analytical tools, explored gas production alternatives to recover methane from fine-grained sediments, and presented implications to recoverable gas from hydrate deposits and sediment-well interactions. Salient findings are listed as follows:

- Gas hydrate formation from dissolved gas is inherently gas limited. Small pores in fine-grained sediments and the finite space in small pores inhibit hydrate nucleation due to the limited amount of dissolved gas present in a single pore. In addition, small pores result in a low hydraulic conductivity and high capillary effect. Low hydraulic conductivity limits the gas supply to the hydrate formation front to diffusive transport. The capillary effect of hydrate and water influences both the chemical and mechanical balance between hydrate mass and the environment. The chemical consequence of the capillary effect is that hydrates with curved surfaces are in a relatively unstable state in comparison to hydrates with flat surfaces.
- A hydrate mass with curved surfaces experiences higher pressure than the surrounding water. This unbalanced pressure reacts on the soil skeleton. Consequently, hydrate formation consolidates the sediments due to cryogenic suction. When the capillary pressure exceeds the effective stress, hydrate mass displaces soil particles and exhibit a segregated morphology.
- The capillary effect of water and gas could generate gas-driven openings in the sediments. Consequently, methane supply to the hydrate formation front could be either through diffusion dominated dissolved methane transport or through gas-driven openings. Hydrate formation by diffusion-controlled methane supply can exhibit Liesegang bands. Hydrate formation in gas-filled openings exhibits two patterns: a hydrate shell along gas-sediments interface and an exo-pore pattern.
- Hydrate formation in fine-grained sediments is subject to the limitation in nucleation, the capillary effect and the slow supply rate of guest molecules. Sufficient temperature depression overcomes capillary effects. Therefore, laboratory experiments focus on the exploration of different strategies to accelerate the guest molecule supply to the gas hydrate formation front. These strategies include the use of THF as guest molecules, the selection of intra-porous diatoms for local gas storage, and gas injection directly into the sediments. In addition, we use long-term

experiments to study diffusion-controlled hydrate formation and ice-hydrate transformation experiments for controlled nucleation topology.

- Gas hydrate can form in fine-grained sediments in laboratory conditions with appropriate strategies to guarantee continuous contact between gas and water, although it is challenging and slow in fine-grained sediments.
- Freshly formed hydrate with large quantities in fine-grained sediments is highly porous.
- Gas driven fractures relax the compression at the opening tip, increase the local void ratio and facilitate hydrate invasion into the sediments.
- The formed hydrate accumulations do not inherit the original morphology of the ice in ice-hydrate transformation experiments: hydrate grows around the first nuclei on the surface of ice lenses and combines supplied gas with extracted water around the nuclei.
- Laboratory and in-situ measurements of physical properties require devices and protocols under high-pressure and low-temperature conditions. In addition, the mismatch between the measurements scale and the representative specimen size could result in biased results. Therefore, theoretical models and numerical experiments are critical in the estimation of the physical properties of hydrate-bearing fine-grained sediments.
- Cryogenic suction during hydrate formation over consolidates the sediments and alters their physical properties.
- Capillarity plays a critical role in gas production from fine-grained sediments. Gas production in fine-grained sediments that use conventional good techniques is not technically viable. Chemical stimulation and CO_2-CH_4 replacement in fine-grained sediments are inefficient and uneconomical. Surface mining in shallow sediments combined with thermal stimulation is a potential method to produce gas from fine-grained hydrate-bearing sediments.
- Analytical solutions explicitly show the interplay between dimensionless ratios defined by the terminal radius/distance and the effective well diameter or strata-bound reservoir geometry, the relative permeability of the sediment with and without hydrates and the permeability of the seal layer, and the extent of depressurization at the well relative to the pressure at the phase boundary and in the far field.

- The size of the production zone or terminal radius/distance increases when the in situ fluid pressure is close to the phase boundary, when high depressurization is imposed at the well, in sediments with high hydrate saturation, in tight aquitard layers, and in thick reservoirs bound between thick aquitard layers. The dissociation distance increases when wells are drilled along the reservoir horizon; then, the affected volume is proportional to the length of the well in the formation.
- Hydro-mechanically coupled analysis must capture the circular link between depressurization → increased effective stress → sediment compaction → reduced hydraulic conductivity due to compaction → altered pressure field, and so on.
- Hydro-mechanical coupling plays a critical role in sediment-well response when soft sediments are subjected to high depressurization. A compacted low-permeability shell forms against the screen/pack. This shell reduces the size of the region affected by depressurization, the potential for gas production, and overall settlement. In fact, the higher the sensitivity of hydraulic conductivity to compaction, the narrower the production zone becomes.
- High compressive axial forces arise in the casing; the maximum compressive force develops within the production horizon. Compression may cause the casing to yield and even collapse. The assumption of a constant hydraulic conductivity leads to a gross overestimation of the axial force in the casing.
- A tensile force develops in the casing above the production horizon as the compacted sediment in the depressurized volume pulls down from the well. The maximum tensile force occurs before steady-state conditions are reached.
- The engineering design of wells used for depressurization in soft sediments should: (1) accommodate extensional displacement in the well above the production horizon, e.g., with slip joints; (2) create soft screen conditions to avoid the buildup of compressive axial force in the casing within the production horizon, e.g., telescopic, sliding or folding design, and (3) incorporate an enlarged gravel pack around the screen to extend the production zone. Horizontal wells minimize the generation of compressive axial forces; however, they remain affected by other hydro-mechanical coupled effects.
- Laboratory tests of hydrate dissociation in fine-grained sediments under low stress show that gas-driven fractures during hydrate dissociation remain open and serve as easy paths for gas percolation until the end of the gas production. However, gas percolation modes in fine-grained sediments subjected to high effective stress remain elusive and need further experimental studies.

7. Related activities

7.1 Training of highly qualified personnel

- Dr. Jang, Junbong (2014). Thesis: Gas-charged sediments: phenomena and characterization. Now at USGS.
- Dr. Terzariol, Marco (2015). Laboratory and field characterization of hydrate-bearing sediments – implications. Now a postdoc at KAUST.
- Dr. Lei, Liang (2017). Thesis: Gas hydrate in fine-grained sediments. Now a postdoc at NETL.
- Dr. Park, Jonghee. Thesis defense in 12/2017
- Mr. Mallet, Seth, Ph.D. in progress
- Mr. Sun, Zhonghao, Ph.D. in progress
- Mr. Kim, Jongchan, Ph.D. in progress

7.2 Journal publications

- Dai, S., Santamarina, J.C., Waite, W.F. and Kneafsey, T.J., (2012). Hydrate morphology: Physical properties of sands with patchy hydrate saturation. *Journal of Geophysical Research: Solid Earth*, 117(B11).
- Dai, S., Wuttke, F. and Santamarina, J.C., (2013). Coda wave analysis to monitor processes in soils. *Journal of Geotechnical and Geoenvironmental Engineering*, 139(9), pp.1504-1511.
- Dai, S. and Santamarina, J.C., (2013). Water retention curve for hydrate-bearing sediments. *Geophysical Research Letters*, 40(21), pp.5637-5641.
- Jang, J. and Santamarina, J.C., (2014). Evolution of gas saturation and relative permeability during gas production from hydrate-bearing sediments: Gas invasion vs. gas nucleation. *Journal of Geophysical Research: Solid Earth*, 119(1), pp.116-126.
- Dai, S., Lee, J.Y. and Santamarina, J.C., (2014). Hydrate nucleation in quiescent and dynamic conditions. *Fluid Phase Equilibria*, 378, pp.107-112.
- Viggiani, G., Andò, E., Takano, D. and Santamarina, J.C., (2014). Laboratory X-ray tomography: A valuable experimental tool for revealing processes in soils. *Geotechnical Testing Journal*, 38(1), 2015, pp. 61-71
- Dai, S. and Santamarina, J.C., (2014). Sampling disturbance in hydrate-bearing sediment pressure cores: NGHP-01 expedition, Krishna–Godavari Basin example. *Marine and Petroleum Geology*, 58, pp.178-186.
- Jang, J. and Santamarina, J. C. (2015). Fines Classification Based on Sensitivity to Pore-Fluid Chemistry. *Journal of Geotechnical and Geoenvironmental Engineer-*

ing, 142(4), 06015018.

- Jang, J. and Santamarina, J.C., (2016). Hydrate bearing clayey sediments: Formation and gas production concepts. *Marine and Petroleum Geology*, 77, pp.235-246.
- Dai, S., Shin, H. and Santamarina, J.C., (2016). Formation and development of salt crusts on soil surfaces. *Acta Geotechnica*, 11(5), pp.1103-1109.
- Jang, J., Sun, Z. and Santamarina, J.C., (2016). Capillary pressure across a pore throat in the presence of surfactants. *Water Resources Research*. 52(12): 9586-9599.
- Dai, S., and Santamarina, J.C., (2017). Stiffness evolution in frozen sands subjected to stress changes. *Journal of Geotechnical and Geoenvironmental Engineering* 143(9), 04017042.
- Park, J., and Santamarina, J. C. (2017). Revised Soil Classification System for Coarse-Fine Mixtures. *Journal of Geotechnical and Geoenvironmental Engineering*, 143(8), 04017039.
- Shin, H. and Santamarina, J.C., (2017). Sediment–well interaction during depressurization. *Acta Geotechnica*, 8, pp.1-13.
- Terzariol, M., Goldsztein, G. and Santamarina, J.C., (2017). Maximum recoverable gas from hydrate bearing sediments by depressurization. *Energy*, 141, pp.1622-1628.
- Ren, X.W. and Santamarina, J.C., (2017). The hydraulic conductivity of sediments: A pore size perspective. *Engineering Geology*, 233: 48-54.
- Lei, L., Santamarina, J. C. Hydrate formation in fine-grained sediments – a laboratory study. *Journal of Geophysical Research* (under review)
- Liu, Z., Kim, J., and Dai, S. THF hydrate in clayey sediments: formation, morphology, and elastic properties. (In preparation)

Reference

Adamson, A.W. and Gast, A.P., 1967. Physical chemistry of surfaces.

Anderson, G.K., 2003. Enthalpy of dissociation and hydration number of carbon dioxide hydrate from the Clapeyron equation. The Journal of Chemical Thermodynamics, 35(7): 1171-1183.

Baez, L.A. and Clancy, P., 1994. Computer simulation of the crystal growth and dissolution of natural gas hydrates. Annals of the New York Academy of Sciences, 715(1): 177-186.

Boswell, R., 2009. Is Gas Hydrate Energy Within Reach? Science, 325(5943): 957-958.

Boswell, R. and Collett, T., 2006. The gas hydrates resource pyramid. Natural Gas & Oil, 304: 285-4541.

Boswell, R. and Collett, T.S., 2011. Current perspectives on gas hydrate resources. Energy & environmental science, 4(4): 1206-1215.

Cha, S.B., Ouar, H., Wildeman, T.R. and Sloan, E.D., 1988. A third-surface effect on hydrate formation. The Journal of Physical Chemistry, 92(23): 6492-6494.

Chand, S., Minshull, T.A., Gei, D. and Carcione, J.M., 2004. Elastic velocity models for gas-hydrate-bearing sediments—A comparison. Geophysical Journal International, 159(2): 573-590.

Chong, S.-H. and Santamarina, J.C., 2016. Soil Compressibility Models for a Wide Stress Range. Journal of Geotechnical and Geoenvironmental Engineering, 142(6): 06016003.

Clennell, B.M., Hovland, M., Booth, J.S., Henry, P. and Winters, W.J., 1999a. Formation of natural gas hydrates in marine sediments 1. Conceptual model of gas hydrate growth conditioned by host sediment properties. J. Geophys. Res., 104(B10): 22985-23003.

Clennell, M.B., Hovland, M., Booth, J.S., Henry, P. and Winters, W.J., 1999b. Formation of natural gas hydrates in marine sediments: 1. Conceptual model of gas hydrate growth conditioned by host sediment properties. Journal of Geophysical Research: Solid Earth, 104(B10): 22985-23003.

Collett, T., Riedel, M., Cochran, J., Boswell, R., Kumar, P., Sathe, A. and Party, T.N.E.S., 2008. Indian continental margin gas hydrate prospects: results of the Indian National Gas Hydrate Program (NGHP) Expedition 01, Proceedingsof the 6th International Conference on Gas Hydrates (ICGH 2008), Vancouver, British Columbia, Canada.

Cook, A.E., Anderson, B.I., Malinverno, A., Mrozewski, S. and Goldberg, D.S., 2010. Electrical anisotropy due to gas hydrate-filled fractures. Geophysics, 75(6): F173-F185.

Cook, A.E., Anderson, B.I., Rasmus, J., Sun, K., Li, Q., Collett, T.S. and Goldberg, D.S., 2012. Electrical anisotropy of gas hydrate-bearing sand reservoirs in the Gulf of Mexico. Marine and Petroleum Geology, 34(1): 72-84.

Cussler, E.L., 2009. Diffusion: mass transfer in fluid systems. Cambridge university press.

Cygan, R.T., Liang, J.-J. and Kalinichev, A.G., 2004. Molecular models of hydroxide, oxyhydroxide, and clay phases and the development of a general force field. The Journal of Physical Chemistry B, 108(4): 1255-1266.

Dai, S., Santamarina, J.C., Waite, W.F. and Kneafsey, T.J., 2012. Hydrate morphology: Physical properties of sands with patchy hydrate saturation. Journal of Geophysical Research: Solid Earth 117(B11): B11205.

Dallimore, S., Yamamoto, K., Wright, J. and Bellefleur, G., 2012. Scientific results from the JOGMEC/NRCan/Aurora Mallik 2007-2008 Gas Hydrate Production Research Well Program, Mackenzie Delta, Northwest Territories, Canada.

Gardner, J.V., Malik, M. and Walker, S., 2009. Plume 1400 Meters High Discovered at the Seafloor off the Northern California Margin. Eos, Transactions American Geophysical Union, 90(32): 275-275.

Ghosh, R., Sain, K. and Ojha, M., 2010. Effective medium modeling of gas hydrate-filled fractures using the sonic log in the Krishna-Godavari basin, offshore eastern India. Journal of Geophysical Research: Solid Earth, 115(B6): B06101.

Handa, Y.P. and Stupin, D.Y., 1992. Thermodynamic properties and dissociation characteristics of methane and propane hydrates in 70-.ANG.-radius silica gel pores. The Journal of Physical Chemistry, 96(21): 8599-8603.

Hofmann, D., Preuss, G. and Mätzler, C., 2015. Evidence for biological shaping of hair ice. Biogeosciences, 12(14): 4261-4273.

Hovland, M., Lysne, D. and Whiticar, M., 1995. Gas hydrate and sediment gas composition, hole 892A1, Proceedings of the Ocean Drilling Program, Scientific Results.

Hunter, R.B., Collett, T.S., Boswell, R., Anderson, B.J., Digert, S.A., Pospisil, G., Baker, R. and Weeks, M., 2011. Mount Elbert gas hydrate stratigraphic test well, Alaska North Slope: Overview of scientific and technical program. Marine and Petroleum Geology, 28(2): 295-310.

Jang, J. and Santamarina, J.C., 2016. Hydrate bearing clayey sediments: Formation and gas production concepts. Marine and Petroleum Geology, 77: 235-246.

Jang, J., Sun, Z. and Santamarina, J.C., 2016. Capillary pressure across a pore throat in the presence of surfactants. Water Resources Research, 52(12): 9586-9599.

Kumar, P., Collett, T.S., Boswell, R., Cochran, J.R., Lall, M., Mazumdar, A., Ramana, M.V., Ramprasad, T., Riedel, M. and Sain, K., 2014. Geologic implications of gas hydrates in the offshore of India: Krishna–Godavari Basin, Mahanadi Basin, Andaman Sea, Kerala–Konkan Basin. Marine and Petroleum Geology, 58: 29-98.

Lee, M. and Collett, T., 2005. Assessments of gas hydrate concentrations estimated from sonic logs in the JAPEX/JNOC/GSC et al. Mallik 5L-38 gas hydrate research production well. Bulletin-Geological Survey of Canada, 585: 118.

Lee, M.W. and Collett, T.S., 2009. Gas hydrate saturations estimated from fractured reservoir at Site NGHP-01-10, Krishna-Godavari Basin, India. J. Geophys. Res., 114(B7): B07102.

Li, Y. and Somorjai, G.A., 2007. Surface Premelting of Ice. The Journal of Physical Chemistry C, 111(27): 9631-9637.

Luan, X., Jin, Y., Obzhirov, A. and Yue, B., 2008. Characteristics of shallow gas hydrate in Okhotsk Sea. Science in China Series D: Earth Sciences, 51(3): 415-421.

McDonald, J.E., 1953. Homogeneous nucleation of supercooled water drops. Journal of Meteorology, 10(6): 416-433.

Merino, E., 1984. Survey of geochemical self-patterning phenomena, Chemical instabilities. Springer, pp. 305-328.

Moridis, G.J., 2008. Toward production from gas hydrates: current status, assessment of resources, and simulation-based evaluation of technology and potential. Lawrence Berkeley National Laboratory.

Moridis, G.J., Kowalsky, M.B. and Pruess, K., 2007. Depressurization-induced gas production from class-1 hydrate deposits. SPE Reservoir Evaluation & Engineering, 10(05): 458-481.

Østergaard, K.K., Anderson, R., Llamedo, M. and Tohidi, B., 2002. Hydrate phase equilibria in porous media: effect of pore size and salinity. Terra Nova, 14(5): 307-312.

Park, S.-H. and Sposito, G., 2003. Do montmorillonite surfaces promote methane hydrate formation? Monte Carlo and molecular dynamics simulations. The Journal of Physical Chemistry B, 107(10): 2281-2290.

Paull, C.K., Ussler, W., Borowski, W.S. and Spiess, F.N., 1995. Methane-rich plumes on the Carolina continental rise: associations with gas hydrates. Geology, 23(1): 89-92.

Pflaum, R.C., Brooks, J.M., Cox, H.B., Kennicutt II, M.C. and Sheu, D.-D., 1986. Molecular and isotopic analysis of core gases and gas hydrates, deep sea drilling project leg 961

Ramseier, R.O., 1967. Self□Diffusion of Tritium in Natural and Synthetic Ice Monocrystals. Journal of Applied Physics, 38(6): 2553-2556.

Rees, E.V.L., Priest, J.A. and Clayton, C.R.I., 2011. The structure of methane gas hydrate bearing sediments from the Krishna–Godavari Basin as seen from Micro-CT scanning. Marine and Petroleum Geology, 28(7): 1283-1293.

Riedel, M., Collett, T.S., Kumar, P., Sathe, A.V. and Cook, A., 2010. Seismic imaging of a fractured gas hydrate system in the Krishna–Godavari Basin offshore India. Marine and Petroleum Geology, 27(7): 1476-1493.

Segura, J.M. and Carol, I., 2008. Coupled HM analysis using zero□thickness interface elements with double nodes. Part I: Theoretical model. International journal for numerical and analytical methods in geomechanics, 32(18): 2083-2101.

Seshadri, K., Wilder, J.W. and Smith, D.H., 2001. Measurements of equilibrium pressures and temperatures for propane hydrate in silica gels with different pore-size distributions. The Journal of Physical Chemistry B, 105(13): 2627-2631.

Shin, H. and Santamarina, J.C., 2011. Open-mode discontinuities in soils, Géotechnique Letters, pp. 95-99.

Sloan, E.D. and Koh, C.A., 2008. Clathrate hydrates of natural gases. CRC Press, Boca Raton.

Sposito, G., Skipper, N.T., Sutton, R., Park, S.-h., Soper, A.K. and Greathouse, J.A., 1999. Surface geochemistry of the clay minerals. Proceedings of the National Academy of Sciences, 96(7): 3358-3364.

Suess, E., Torres, M., Bohrmann, G., Collier, R., Rickert, D., Goldfinger, C., Linke, P., Heuser, A., Sahling, H. and Heeschen, K., 2001. Sea floor methane hydrates at Hydrate Ridge, Cascadia margin. Natural gas hydrates: occurrence, distribution, and detection: 87-98.

Sultan, N., Bohrmann, G., Ruffine, L., Pape, T., Riboulot, V., Colliat, J.L., De Prunelé, A., Dennielou, B., Garziglia, S., Himmler, T., Marsset, T., Peters, C.A., Rabiu, A. and Wei, J., 2014. Pockmark formation and evolution in deep water Nigeria: Rapid

hydrate growth versus slow hydrate dissolution. Journal of Geophysical Research: Solid Earth, 119(4): 2679-2694.
Sultan, N., Foucher, J.-P., Cochonat, P., Tonnerre, T., Bourillet, J.-F., Ondreas, H., Cauquil, E. and Grauls, D., 2004. Dynamics of gas hydrate: case of the Congo continental slope. Marine Geology, 206(1): 1-18.
Taylor, C.J., Miller, K.T., Koh, C.A. and Sloan, E.D., 2007. Macroscopic investigation of hydrate film growth at the hydrocarbon/water interface. Chemical Engineering Science, 62(23): 6524-6533.
Terzariol, M., Goldsztein, G. and Santamarina, J., 2017. Maximum recoverable gas from hydrate bearing sediments by depressurization. Energy, 141: 1622-1628.
Uchida, T., Ebinuma, T. and Ishizaki, T., 1999a. Dissociation condition measurements of methane hydrate in confined small pores of porous glass. The Journal of Physical Chemistry B, 103(18): 3659-3662.
Uchida, T., Ebinuma, T., Kawabata, J.i. and Narita, H., 1999b. Microscopic observations of formation processes of clathrate-hydrate films at an interface between water and carbon dioxide. Journal of crystal growth, 204(3): 348-356.
Waite, W.F., Santamarina, J.C., Cortes, D.D., Dugan, B., Espinoza, D.N., Germaine, J., Jang, J., Jung, J.W., Kneafsey, T.J., Shin, H., Soga, K., Winters, W.J. and Yun, T.S., 2009. Physical properties of hydrate-bearing sediments. Reviews of Geophysics, 47(4): RG4003.
Watanabe, K., Yokokawa, K. and Muto, Y., 2006. Observation of Frost Heave of THF Clathrate Hydrate on Porous Glass Powder. In: M. Davies and J.E. Zufelt (Editors). ASCE, Orono, Maine, USA, pp. 44-44.
Westacott, R.E. and Rodger, P.M., 1998. A local harmonic study of clusters of water and methane. Journal of the Chemical Society, Faraday Transactions, 94(23): 3421-3426.
Wood, W., Gettrust, J., Chapman, N., Spence, G. and Hyndman, R., 2002. Decreased stability of methane hydrates in marine sediments owing to phase-boundary roughness. Nature, 420(6916): 656-660.
Xu, W. and Ruppel, C., 1999. Predicting the occurrence, distribution, and evolution of methane gas hydrate in porous marine sediments. J. Geophys. Res., 104.
Yamamoto, K., Terao, Y., Fujii, T., Ikawa, T., Seki, M., Matsuzawa, M. and Kanno, T., 2014. Operational overview of the first offshore production test of methane hydrates in the Eastern Nankai Trough, Offshore Technology Conference. Offshore Technology Conference.
Yun, T.S., Lee, C., Lee, J.-S., Bahk, J.J. and Santamarina, J.C., 2011a. A pressure core based characterization of hydrate-bearing sediments in the Ulleung Basin, Sea of Japan (East Sea). J. Geophys. Res., 116(B2): B02204.
Yun, T.S., Lee, C., Lee, J.-S., Bahk, J.J. and Santamarina, J.C., 2011b. A pressure core based characterization of hydrate-bearing sediments in the Ulleung Basin, Sea of Japan (East Sea). Journal of Geophysical Research: Solid Earth, 116(B2): B02204.

National Energy Technology Laboratory

626 Cochrans Mill Road
P.O. Box 10940
Pittsburgh, PA 15236-0940

3610 Collins Ferry Road
P.O. Box 880
Morgantown, WV 26507-0880

13131 Dairy Ashford Road, Suite 225
Sugar Land, TX 77478

1450 Queen Avenue SW
Albany, OR 97321-2198

Arctic Energy Office
420 L Street, Suite 305
Anchorage, AK 99501

Visit the NETL website at:
www.netl.doe.gov

Customer Service Line:
1-800-553-7681